Anderson localization in strongly coupled disordered electron–phonon systems

FRANZ X. BRONOLD†, ANDREAS ALVERMANN‡ and HOLGER FEHSKE†

†Institut für Physik, Ernst-Moritz-Arndt-Universität Greifswald, D-17487
Greifswald, Germany
‡Physikalisches Institut, Universität Bayreuth, D-95440 Bayreuth, Germany

ABSTRACT

Based on the statistical dynamic mean-field theory, we investigate, in a generic model for a strongly coupled disordered electron–phonon system, the competition between polaron formation and Anderson localization. The statistical dynamic mean-field approximation maps the lattice problem to an ensemble of self-consistently embedded impurity problems. It is a probabilistic approach, focusing on the distribution instead of the average values for observables of interest. We solve the self-consistent equations of the theory with a Monte Carlo sampling technique, representing distributions for random variables by random samples, and discuss various ways to determine mobility edges from the random sample for the local Green function. Specifically, we give, as a function of the 'polaron parameters', such as adiabaticity and electron–phonon coupling constants, a detailed discussion of the localization properties of a single polaron, using a bare electron as a reference system.

§1. INTRODUCTION

There is a large variety of materials in which, because of strong electron–phonon coupling, electrons and phonons lose their identity and form new composite entities: polarons. Examples of current interest are, among others, the high-temperature superconducting perovskites (Bar-Yam *et al.* 1992, Salje *et al.* 1995), the non-metallic nickelates and bismuthates (Cheong *et al.* 1994, Oyanagi and Bianconi 2001), the colossal magnetoresistance manganites (Jin *et al.* 1994, Tokura and Tomioka 1999) and semiconducting molecular crystals (Parris *et al.* 2001). In all these materials, electronic properties, for instance the electronic spectral function or the optical conductivity, show substantial polaronic effects. The most important signature in this respect is thermally activated transport (along at least one of the crystallographic axes).

The polaron concept was introduced by Landau (1933) and has played a central role in the analysis of strongly coupled electron–phonon systems ever since. In a deformable lattice, the coupling between an electron and the lattice leads to a lattice deformation whose potential tends to bind the electron. This process is called self-trapping, because the potential depends on the state of the electron (Firsov 1975,

Rashba 1982, Wellein and Fehske 1998). Translational symmetry is not broken in this process, transport at low enough temperatures is still coherent and band-like, with a much larger mass, however, because of the lattice distortion that the electrons have to carry. The self-trapping process, that is the formation of polarons, is therefore only the crossover from a weakly dressed electronic quasiparticle to a heavily dressed polaronic quasiparticle. Even the small polaron, although much less mobile than the bare electron, is still itinerant and not localized.

Details of the actual materials notwithstanding, the Holstein (1959) model, which describes electrons locally coupled to dispersionless phonons, captures the essence of the self-trapping process. Most of the theoretical work is therefore directly based on the Holstein model (DeRaedt and Lagendijk 1983, Ranninger and Thibblin 1992, Marsiglio 1993, Alexandrov *et al.* 1994, Stephan 1996, Wellein *et al.* 1996, Capone *et al.* 1997, Bonča *et al.* 1999). Extensions to long-range electron–phonon couplings on a discrete lattice were discussed by Alexandrov and Kornilovitch (1999) and by Fehske *et al.* (2000). Despite the extensive numerical simulations, the properties of the Holstein model are not yet fully understood, especially at finite densities, where the situation changes because of the interaction between polarons. Even in the extreme dilute limit, where polarons as a first approximation do not interact, many questions remain. For instance, little is quantitatively known about polaron formation in a disordered environment.

On the other hand, polaronic materials are complex materials, where chemical as well as crystallographic imperfections can be quite substantial. Accordingly, the self-trapping process, producing a heavy quasiparticle, occurs in an environment where, strictly speaking, translational symmetry is broken, and where defects most probably act as nucleation sites for the formation of polarons. Therefore, a complete theory of polaron formation has to take the disordered environment into account. In particular, the notoriously difficult question of whether polaron states are band states or localized defect states can only be meaningfully addressed in a context which takes the most important effect due to disorder, the possibility of Anderson localization, explicitly into account.

In his seminal work, Anderson (1958) showed that disorder, if sufficiently strong, dramatically changes the properties of the electronic states in a solid. Whereas for small disorder the electronic states are extended Bloch waves, for large disorder the electronic states are localized defect states. Anderson localization, that is the transition from extended to localized states, is well understood for non-interacting electrons (see, for instance, the review articles by Thouless (1974), Brezini and Zerki (1992) and Kramer and MacKinnon (1993)). It depends strongly on dimensionality. In one dimension (and arguably in two dimensions (Abrahams *et al.* 1979)), localized and extended states cannot coexist, because infinitesimally small disorder suffices to localize all states at once whereas, in three dimensions, mobility edges separate localized from extended states. Since the mobility edge is of utmost importance for the transport properties (Mott 1968a,b, 1976, 1981), an enormous amount of experimental and theoretical effort has been directed towards a precise determination of its position.

That Anderson localization might affect polaron formation, and vice versa, has been emphasized several times, starting with Anderson (1972) himself, who pointed out that the mobility edge might be surrounded by self-trapped states. Not much quantitative work exists, however, to determine, for instance, the position of the mobility edge and its consequences for the conductivity (Girvin and Jonson 1980,

Mueller and Thomas 1983), or the character of the states near the mobility edge (Cohen *et al.* 1983) taking electron–phonon coupling explicitly into account. Despite some occasionally fruitful adaptations of techniques from nonlinear dynamics (Kopidakis *et al.* 1996), where polaron formation is considered as an intrinsic interaction-driven nonlinearity, the precise mechanisms of the interplay of Anderson localization and polaron formation are essentially unknown.

As a first step to address this problem with techniques developed in the field of strongly correlated electron systems, Bronold *et al.* (2001) applied the dynamic mean-field theory (DMFT) (Georges *et al.* 1996) to study a single electron in the Holstein model with binary disorder, focusing especially on polaron states at the high-energy edge of the lowest polaronic subband. These states are extremely sensitive to disorder, with a return probability which, owing to the phonon admixture, is several orders of magnitude larger than for the states at the bottom of the subband. Within the DMFT it was, however, impossible to determine the critical disorder needed to localize polaron states. Accordingly, mobility edges for polaron states could not be determined.

To overcome the limitations of the DMFT, we adopted therefore a recently proposed generalization of the DMFT, the statistical dynamic mean-field theory (statDMFT) (Dobrosavljević and Kotliar 1997, 1998), to the Holstein model with uniformly distributed on-site energies (Bronold and Fehske 2002, 2003). The statDMFT is capable of accounting for not only the polaron formation process but also the spatial fluctuations giving rise to Anderson localization. Within the statDMFT we could clearly distinguish between itinerant and localized polaron states. The purpose of this paper is to give an extended account of our investigations, with a complete description of the technical apparatus, including the details of the numerical implementation of the statDMFT, and a full discussion of the localization properties of a single polaron.

As a generic model for a disordered polaronic material, we use the Anderson–Holstein model (AHM)

$$H = \sum_{i\sigma} \epsilon_i n_{i\sigma} - \sum_{i,j,\sigma} J_{ij} c_{i\sigma}^\dagger c_{j\sigma} + \Omega \sum_i b_i^\dagger b_i - (E_{\mathrm{p}}\Omega)^{1/2} \sum_{i\sigma} (b_i + b_i^\dagger) n_{i\sigma}, \qquad (1)$$

where $c_{i\sigma}^\dagger (b_i^\dagger)$ are electron (phonon) creation operators, $n_{i\sigma} = c_{i\sigma}^\dagger c_{i\sigma}$ is the electron density on site i, the electron transfer integral $J_{ij} = J$ for (i, j) next-neighbour sites and zero otherwise, Ω is the bare phonon energy ($\hbar = 1$) and E_{p} is the polaron shift. The on-site energies $\{\epsilon_i\}$ are assumed to be independent, identically distributed random variables with a uniform distribution $p(\epsilon_i) = (1/\gamma)\theta(\gamma/2 - |\epsilon_i|)$.

The 'polaron properties' of the AHM are governed by two parameter ratios: the adiabaticity $\alpha = \Omega/J$, indicating whether the polaron is light ($\alpha \ll 1$) or heavy ($\alpha \gg 1$) (Rashba 1982, Wellein and Fehske 1998), and a dimensionless electron–phonon coupling constant $\lambda = E_{\mathrm{p}}/2J$ or $g^2 = E_{\mathrm{p}}/\Omega$. Polaron formation sets in if both $\lambda > 1$ and $g^2 > 1$. The internal structure of the polaronic quasi-particle depends on α, in particular the momentum-dependent phonon admixture. It is quite different in the adiabatic ($\alpha \ll 1$), non-adiabatic ($\alpha \approx 1$) and anti-adiabatic ($\alpha \gg 1$) regimes. Another important effect occurs in the intermediate-coupling regime, where electron–phonon coupling initiates long-range tunnelling processes (Fehske *et al.* 1997a, b). Evidently, how disorder affects polaron states strongly depends on the polaron parameters. As a result, the 'localization properties' are expected to be quite different in the various polaronic regimes.

The strength of disorder is specified by the width γ of the distribution for the on-site energy ϵ_i. The structure of the AHM suggests that two regimes can be distinguished. The weakly disordered Holstein regime, where γ is small on the scale of the bare bandwidth and the strongly disordered Anderson regime, with γ large on the scale of the width of the polaronic subbands.

The organization of the paper is as follows. In §2 a general description of the statDMFT is given. As a guidance, we first put in §2.1 our work and the statDMFT into perspective. For electrons interacting with phonons, the basic equations are derived in §2.2. The statDMFT reduces for lattices with a large coordination number to the DMFT. This is shown in Appendix A. For practical calculations it is convenient to use a Bethe lattice. Therefore in §2.3 the basic equations are specified for the Bethe lattice. Finally the localization criterion used to identify localized states is introduced in §2.4. Numerical results in the single-particle sector are presented in §3. After specializing the basic equations in §3.1 to the case of a single particle at zero temperature, we first give in §3.2 the results with electron–phonon coupling turned off. The pure Anderson case serves two purposes: firstly, it demonstrates, for a well-understood case, that the method and the localization criterion work; secondly, it is used as a reference point for the analysis of the polaron case presented in §3.3. Finally, we conclude in §4 with a short outlook.

§2. STATISTICAL DYNAMIC MEAN-FIELD THEORY

2.1. *General considerations*

Before we go into technical details, we put our work and the statDMFT into perspective. Self-trapping in a disordered environment is one example of physical problems where interaction and disorder effects interfere with each other. The most prominent example is electron transport in the impurity band of doped semiconductors. Especially near the metal–insulator transition, Coulomb interaction and disorder effects cannot be separated, and it is suspected that it is precisely the interplay of both that leads to new physical phenomena, for instance, to the formation of local moments (Finkel'stein 1983, Castellani *et al.* 1984) or to a new emerging magnetic phase (Kirkpatrick and Belitz 1990).

There is no method that could be mechanically used to investigate disordered interacting systems beyond perturbation theory. In particular, the strongly disordered regime, where Anderson localization takes place, is beyond the applicability of most theoretical techniques. Nevertheless, there have been various attempts to generalize methods, which have been successfully employed to investigate Anderson localization of non-interacting electrons in such a way that they can be also utilized in situations where interactions are important. Most efforts have been directed towards electrons interacting via short- and/or long-range Coulomb potentials, with a few exceptions dealing with electrons coupled to phonons (Anderson 1972, Girvin and Jonson 1980, Cohen *et al.* 1983, Mueller and Thomas 1983, Kopidakis *et al.* 1996, Bronold *et al.* 2001, Bronold and Fehske 2002, 2003).

After Anderson's (1958) original work and Mott's (1968a, b, 1976, 1981) suggestion of its connection to transport properties in amorphous semiconductors, three major techniques have been cultivated to study Anderson localization quantitatively in further detail:

(i) direct numerical simulations (see, for example, the review articles by Thouless (1974), Brezini and Zerki (1992) and Kramer and MacKinnon (1993));

(ii) diagrammatic techniques (Vollhardt and Wölfle 1980) (for recent studies consult also the review articles by Kramer and MacKinnon (1993) and Vollhardt and Wölfle (1992));

(iii) field-theoretical approaches (Wegner 1976) (for recent studies consult Kramer and MacKinnon (1993)).

Subsequently, all three techniques have been applied to interacting systems as well. Direct numerical simulations are conceptually the simplest approach. However, they are restricted to small system sizes and usually to a truncated configuration-type treatment of the Coulomb interaction. To this category belong, for instance, all attempts to study the localization of two interacting electrons in the background of a frozen Fermi sea (von Oppen *et al.* 1996). In the case of electron–phonon interaction, the size of the phonon Hilbert space is the limiting factor. Diagrammatic methods usually work only for weak interactions (Lee and Ramakrishnan 1985). In principle, strong interactions can be also treated with diagrammatic techniques, if they are based on renormalized expansions, but the proliferation of diagrams makes the practical implementation very often rather complicated if not impossible. Field-theoretical techniques, in contrast, for instance based on the construction of an effective-field theory for the low-energy long-wavelength excitations (Belitz and Kirkpatrick 1994, Kamenev and Andreev 1999), albeit very promising, operate in abstract spaces, with order parameter functions whose physical content is sometimes hard to grasp.

Anderson (1958), on the other hand, used a completely different approach. Instead of focusing on the calculation of averaged correlation functions, he emphasized that, in general, average values are not representative, especially in the strongly disordered regime. All variables of the theory and, in particular, observables, should be characterized by distributions. Specifically, he examined, in probabilistic terms, the convergence properties of the renormalized perturbation series for the local hybridization function appearing in a locator expansion of the local Green function. Towards that end, he gave asymptotic estimates for the higher-order terms of the series. The mathematical arguments are quite involved and have been further clarified later, most notably by Thouless (1970, 1974) and Economou and Cohen (1972). A simplified probabilistic approach, based on the self-consistent solution of the second-order renormalized perturbation series, started with Abou-Chacra *et al.* (1973). It proved to be a very powerful tool, applicable not only to substitutionally (Kumar *et al.* 1975, Brezini 1982, Brezini and Olivier 1983, Miller and Derrida 1993) but also to topologically disordered materials (Heinrichs 1977, Fleishman and Stein 1979, Elyutin 1979, 1981, Logan and Wolynes 1985, 1986, 1987).

The flexibility of the simplified probabilistic analysis of the renormalized perturbation series has been recently utilized by Dobrosavljević and Kotliar (1997, 1998) to analyse various physical properties of disordered electrons with strong local electron–electron correlations (Miranda and Dobrosavljević 2001a, b, Aguiar *et al.* 2003). They successfully combined the dynamic mean-field approximation for the description of (local) correlations with the probabilistic treatment of the spatial fluctuations due to randomness by Abou-Chacra *et al.* The statDMFT maps the original lattice problem on to an ensemble of impurity problems, which is then analysed in terms of probability. In contrast with the field-theoretical approaches,

the method is very intuitive and conceptually simple. Moreover, it captures local interaction processes non-perturbatively. It is therefore capable of addressing issues beyond standard diagrammatic perturbation theories. Numerically it is somewhat involved, but not restricted to small system sizes as direct numerical simulations. The main drawback of the method is its restriction to local short-range interactions. In principle, long-range interaction processes could be incorporated, but only at the level of static molecular fields (for instance, in the case of Coulomb interaction, a Hartree term would appear), which is probably not sufficient for a complete investigation of the interplay between long-range interactions and disorder. For the AHM, however, where the (electron–phonon) coupling is local, the statDMFT's problem to deal with long-range interactions does not occur and the statDMFT is expected to capture the essential physics of the interplay between Anderson localization and self-trapping.

2.2. *Derivation of the basic equations*

The derivation of the statDMFT for a generic model of interacting electrons has been given by Dobrosavljević and Kotliar (1997, 1998). It is based on the cavity method and applies to arbitrary lattices, temperatures and densities. To make our presentation self-contained and to fix our notation, we outline in this section the cavity method, carefully paying attention to the probabilistic interpretation of the statDMFT and to specifics due to electron–phonon coupling.

The starting point is the partition function

$$Z = \int \prod_{i,\sigma} \mathcal{D}c_{i\sigma}^{\dagger} \, \mathcal{D}c_{i\sigma} \, \mathcal{D}b_i^{\dagger} \, \mathcal{D}b_i \, \mathrm{e}^{-S[c^{\dagger}, c, b^{\dagger}, b]}, \tag{2}$$

where the action, for a fixed realization of the on-site energies, is given by

$$S[c, c^{\dagger}, b, b^{\dagger}] = \int_0^{\beta} \mathrm{d}\tau \sum_{j,\sigma} \left\{ c_{j\sigma}^{\dagger}(\tau)(\partial_{\tau} - \mu)c_{j\sigma}(\tau) + b_j^{\dagger}(\tau)\partial_{\tau}b_j(\tau) + H[c, c^{\dagger}, b, b^{\dagger}](\tau) \right\}. \tag{3}$$

All sites but one are now integrated out, yielding an effective single-site action. For that purpose, the action is split into three parts: $S = S_i + S^{(i)} + \Delta S(i)$, where S_i is the action of the isolated site i; $S^{(i)}$ is the action for the system with site i excluded and

$$\Delta S(i) = -\int_0^{\beta} \mathrm{d}\tau \sum_{l,\sigma} \left[c_{l\sigma}^{\dagger}(\tau)\eta_{l\sigma}(\tau) + \eta_{l\sigma}^{\dagger}(\tau)c_{l\sigma}(\tau) \right], \tag{4}$$

with $\eta_{l\sigma} = J_{li}c_{i\sigma}$, is the part of the action which connects site i to its neighbours.

Identifying $\Delta S(i)$ as a source term to generate cavity Green functions, that is Green functions for the lattice with site i removed, the effective single-site action $S(i)$, defined by

$$\mathrm{e}^{-S(i)} = \frac{1}{Z} \int \prod_{j \neq i, \sigma} \mathcal{D}c_{j\sigma}^{\dagger} \, \mathcal{D}c_{j\sigma} \, \mathcal{D}b_j^{\dagger} \, \mathcal{D}b_j \, \mathrm{e}^{-[S_i + S^{(i)} + \Delta S(i)]}, \tag{5}$$

can be written as

$$S(i) = S_0 + S_i[c_{i\sigma}^{\dagger}, c_{i\sigma}, b_i^{\dagger}, b_i] - W^{(i)}[\eta^{\dagger}, \eta], \tag{6}$$

where we explicitly indicated the fields on which the various terms depend. The first term S_0 is a constant. While the second term, the action for the isolated site i, contains only the fields on site i, the third term

$$W^{(i)}[\eta^\dagger, \eta] = 1 + \sum_n \int_0^\beta d\tau_1 \dots \int_0^\beta d\tau_n \int_0^\beta d\tau_1' \dots \int_0^\beta d\tau_n' A^{[2n]}(\tau_1, \dots, \tau_n'), \tag{7}$$

with

$$\begin{aligned}
A^{[2n]}(\tau_1, \dots, \tau_n') = (-)^n \sum_{l_1, \sigma_1} \dots \sum_{l_n', \sigma_n'} \eta_{l_1\sigma_1}^\dagger(\tau_1) \dots \eta_{l_n\sigma_n}^\dagger(\tau_n) G_{l_1\sigma_1 \dots l_n'\sigma_n'}^{(i)}(\tau_1, \dots, \tau_n') \\
\times \eta_{l_1'\sigma_1'}(\tau_1') \dots \eta_{l_n'\sigma_n'}(\tau_n'),
\end{aligned} \tag{8}$$

involves fields from all sites.

The effective single-site action $S(i)$ contains the full information of the original lattice action. Integrating out all sites but one introduces a $2n$-point cavity Green function $G_{l_1\sigma_1 \dots l_n'\sigma_n'}^{(i)}(\tau_1, \dots, \tau_n')$. This function is extremely involved and approximations are required to obtain feasible equations. A crucial simplification can be made by truncating equation (7) after the $n = 1$ term. This leads to a quadratic effective single-site action, similar to the DMFT (Georges *et al.* 1996), where it was further shown that the truncation becomes exact for lattices with an infinite coordination number. As a consequence, although the cavity construction is performed for lattices with a finite coordination number, interaction processes, here due to the electron–phonon coupling, are treated as if the lattice had an infinite coordination number. As a result of the truncation, the statDMFT becomes a mean-field theory.

Keeping only the $n = 1$ term, equation (7) depends only on the electronic fields on site i and reduces to

$$W^{(i)}[c_{i\sigma}^\dagger, c_{i\sigma}] = 1 - \int_0^\beta d\tau \int_0^\beta d\tau' \sum_\sigma c_{i\sigma}^\dagger(\tau) H_{i\sigma i\sigma}(\tau - \tau') c_{i\sigma}(\tau'), \tag{9}$$

with the hybridization function

$$H_{i\sigma i\sigma}(\tau - \tau') = J^2 \sum_{lm} G_{l\sigma m\sigma}^{(i)}(\tau - \tau'). \tag{10}$$

The information of the lattice is now contained in the two-point cavity Green function $G_{l\sigma m\sigma}^{(i)}(\tau - \tau')$, describing all paths from site l to site m without passing through site i (note that, owing to the definition of J_{lm}, both sites l and m are neighbouring sites to i).

Absorbing irrelevant constants, which do not affect the electron dynamics, into Z_0, the effective single-site action reads

$$\begin{aligned}
S(i) = \int_0^\beta d\tau \, d\tau' \sum_\sigma c_{i\sigma}^\dagger(\tau) \Big\{ (\partial_\tau + \epsilon_i - \mu)\delta(\tau - \tau') + H_{i\sigma i\sigma}(\tau - \tau') \Big\} c_{i\sigma}(\tau') \\
+ S_{\text{ph}}(i) + S_{\text{int}}(i),
\end{aligned} \tag{11}$$

with

$$S_{\text{ph}}(i) = \int_0^\beta d\tau \, b_i^\dagger(\tau)(\partial_\tau + \Omega) b_i(\tau) \tag{12}$$

and

$$S_{\text{int}}(i) = -\int_0^\beta d\tau \, (E_p \Omega)^{1/2} [b_i(\tau) + b_i^\dagger(\tau)] n_{i\sigma}(\tau). \tag{13}$$

According to equation (11), the interaction between electrons and phonons takes place only on site i, which, owing to the hybridization function $H_{i\sigma i\sigma}(\tau)$, is, however, embedded into the full lattice.

Although, for a given $H_{i\sigma i\sigma}(\tau)$, any local Green function could be obtained from $S(i)$, the set of equations is not closed. This can be most clearly seen from the identity (Dobrosavljević and Kotliar 1997, 1998)

$$\int_0^\beta d\tau' \, G_{l\sigma i\sigma}(\tau - \tau') G_{i\sigma m\sigma}(\tau') = \int_0^\beta d\tau' \Big[G_{l\sigma m\sigma}(\tau - \tau') - G_{l\sigma m\sigma}^{(i)}(\tau - \tau') \Big] G_{i\sigma i\sigma}(\tau'), \tag{14}$$

which connects the cavity Green function $G_{l\sigma m\sigma}^{(i)}(\tau)$ with the lattice Green function $G_{l\sigma m\sigma}(\tau)$. Therefore, the hybridization function $H_{i\sigma i\sigma}(\tau)$ defined in equation (10) is a functional of the full non-local lattice Green function, which of course cannot be obtained from the effective single-site action $S(i)$.

To close the set of equations, Dobrosavljević and Kotliar (1997, 1998) suggested approximating in equations (10) and (14), for a given realization of disorder, the full lattice Green function $G_{l\sigma m\sigma}(\tau)$ by the bare lattice Green function $G_{l\sigma m\sigma}^0$, with on-site energies shifted by the local self-energy. In Matsubara space the substitution reads

$$G_{i\sigma j\sigma}(i\omega_n) \to G_{i\sigma j\sigma}^0(i\omega_n) \Big|_{\epsilon_i \to \epsilon_i + \Sigma_{i\sigma}(i\omega_n)}, \tag{15}$$

with $\Sigma_{i\sigma}(i\omega)$ defined by

$$G_{i\sigma i\sigma}(i\omega_n) = \frac{1}{i\omega_n - \epsilon_i + \mu - H_{i\sigma i\sigma}(i\omega_n) - \Sigma_{i\sigma}(i\omega_n)}, \tag{16}$$

which is the Fourier-transformed Dyson equation for the local Green function $G_{i\sigma i\sigma}(\tau) = -\langle T_\tau c_{i\sigma}(\tau) c_{i\sigma}^\dagger(0) \rangle_{S(i)}$ as obtained from the effective single-site action $S(i)$. Note the substitution of equation (15) is not exact, because in general the interaction self-energy is non-local. Besides the truncation of the effective single-site action, this is the second major approximation invoked by the statDMFT.

Now the set of equations (10)–(16) is closed and constitutes the basic statDMFT equations, applicable to arbitrary temperatures, densities and lattices. A self-consistent solution yields the local Green function $G_{i\sigma i\sigma}(i\omega_n)$.

It is crucial to realize that, owing to the randomness of the on-site energies ϵ_i, the local Green function $G_{i\sigma i\sigma}(\tau)$, the local self-energy $\Sigma_{i\sigma}(\tau)$ and the local hybridization function $H_{i\sigma i\sigma}(\tau)$ are random variables. More specifically, interpreting the site indices as labels enumerating the elements of random samples, $G_{i\sigma i\sigma}(\tau)$, $\Sigma_{i\sigma}(\tau)$ and $H_{i\sigma i\sigma}(\tau)$ can be understood as particular realizations of the random variables $G_\sigma^{\text{loc}}(\tau)$, $\Sigma_\sigma^{\text{loc}}(\tau)$, and $H_\sigma^{\text{loc}}(\tau)$ respectively. Thus, equations (10)–(16) are in fact stochastic recursion relations, from which random samples for the random variables $G_\sigma^{\text{loc}}(\tau)$, $\Sigma_\sigma^{\text{loc}}(\tau)$ and $H_\sigma^{\text{loc}}(\tau)$ can be constructed. The iterative solution of equations (10)–(16) is therefore equivalent to the calculation of the distribution for the random variables $G_\sigma^{\text{loc}}(\tau)$, $\Sigma_\sigma^{\text{loc}}(\tau)$ and $H_\sigma^{\text{loc}}(\tau)$.

Starting from an initial sample $\{H_{i\sigma i\sigma}(\tau)\}$ for the local hybridization function $H_\sigma^{\text{loc}}(\tau)$, a sample $\{G_{i\sigma i\sigma}(\tau)\}$ for the local Green function $G_\sigma^{\text{loc}}(\tau)$ is obtained by solving

the quantum-mechanical many-body problem defined by $S(i)$ [cf. equations (11)–(13)]. The Dyson equation (16) for the local Green function yields then a sample $\{\Sigma_{i\sigma}(\tau)\}$ for the local self-energy $\Sigma_\sigma^{\text{loc}}(\tau)$, from which a new sample for the hybridization function is calculated from equations (15), (14) and (10). Going through this loop iteratively, the random samples are successively updated until a fixed point is reached.

The iteration is numerically very involved for Bravais lattices (for instance sc, fcc or bcc lattices), in particular the construction of the lattice Green function through equation (15). In practice, the statDMFT is therefore formulated for a Bethe lattice, which is an infinite loop-free graph with connectivity K (where $K+1$ is the number of next neighbours). Besides the reduced numerical complexity, the Bethe lattice has the additional advantage that the statistical dependence of the random variables can be analysed in detail.

Finally, we mention that the statDMFT reduces to the DMFT for lattices with a large coordination number. For the particular case of a Bethe lattice, this is shown in appendix A.

2.3. *Specification for a Bethe lattice*

Owing to the absence of closed loops, the hybridization function on the Bethe lattice depends only on the *local* cavity Green function, which can again be obtained from an appropriate effective single-site action. As a result, the statDMFT can be simplified enormously for a Bethe lattice.

Specifically for the $K=2$ Bethe lattice with nearest-neighbour coupling shown in figure 1, the hybridization function becomes

$$H_{i\sigma i\sigma}(i\omega_n) = J^2 \sum_{j\,\text{NN}\,i} G_{j\sigma j\sigma}^{(i)}(i\omega_n), \tag{17}$$

where now only local cavity Green functions appear. This is the crucial simplification because $G_{j\sigma j\sigma}^{(i)}(i\omega_n)$ can be obtained from the effective single-site action $S^{(i)}(j)$, which has the same structure as $S(j)$, except that the hybridization function is now given by

$$H_{j\sigma j\sigma}^{(i)}(i\omega_n) = J^2 \sum_{l\neq i\,\text{NN}\,j} G_{l\sigma l\sigma}^{(ji)}(i\omega_n). \tag{18}$$

In addition, for a Bethe lattice, because of the absence of closed loops, the exclusion of site j already ensures that site i is not visited, that is $G_{l\sigma l\sigma}^{(ji)}(i\omega_n) = G_{l\sigma l\sigma}^{(j)}(i\omega_n)$. Accordingly, except for the 'base' site i, the hybridization function for all other sites is simply given by the sum over the 'forward' cavity Green function. For
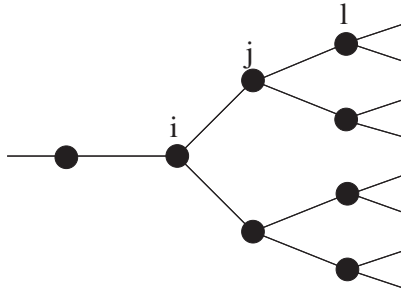

Figure 1. $K=2$ Bethe lattice.

the base site, in contrast, all the neighbouring cavity Green functions contribute (see equation (17)).

As a consequence, taking i as the base site, from which the cavity construction starts, gives for the Dyson equation for the local base site Green function

$$G_{i\sigma i\sigma}(i\omega_n) = \left(i\omega_n + \mu - \epsilon_i - J^2 \sum_{j \, \mathrm{NN} \, i} G^{(i)}_{j\sigma j\sigma}(i\omega_n) - \Sigma_{i\sigma}(i\omega_n)\right)^{-1}, \qquad (19)$$

whereas the Dyson equation for the local Green function at all other sites is

$$G^{(i)}_{j\sigma j\sigma}(i\omega_n) = \left(i\omega_n + \mu - \epsilon_j - J^2 \sum_{l \neq i \, \mathrm{NN} \, j} G^{(j)}_{l\sigma l\sigma}(i\omega_n) - \Sigma^{(i)}_{j\sigma}(i\omega_n)\right)^{-1}. \qquad (20)$$

Note that all cavity Green functions $G^{(i)}_{j\sigma j\sigma}(i\omega_n)$ obey equation (20); hence they are identically distributed. Moreover, because the cavity self-energy $\Sigma^{(i)}_{j\sigma}(i\omega_n)$ is obtained from $S^{(i)}(j)$, containing only 'forward' sites with respect to site j, the cavity Green functions are also statistically independent and $G^{(i)}_{j\sigma j\sigma}(i\omega_n)$ can be interpreted as a particular realization of the random variable $G^{\mathrm{cav}}_\sigma(i\omega_n)$. The statistical dependence between cavity Green functions at different energies is another issue. Naturally, it depends on the interaction processes and the particular approximation employed to calculate the local self-energy (see below).

In principle the base site self-energy $\Sigma_{i\sigma}(i\omega_n)$ and the cavity self-energy $\Sigma^{(i)}_{j\sigma}(i\omega_n)$ are different. If, in the spirit of the DMFT, we neglect, however, this difference and identify $\Sigma_{i\sigma}(i\omega_n)$ with $\Sigma^{(i)}_{j\sigma}(i\omega_n)$, equation (19) reduces for i and j next-neighbour sites to

$$G_{i\sigma i\sigma}(i\omega_n) = \frac{1}{[G^{(j)}_{i\sigma i\sigma}(i\omega_n)]^{-1} - J^2 G^{(i)}_{j\sigma j\sigma}(i\omega_n)}. \qquad (21)$$

Within this approximation, the local Green function $G_{i\sigma i\sigma}(i\omega_n)$ is expressed in terms of two statistically independent random variables: $G^{(j)}_{i\sigma i\sigma}(i\omega_n)$ and $G^{(i)}_{j\sigma j\sigma}(i\omega_n)$. The identification of $\Sigma_{j\sigma}(i\omega_n)$ with $\Sigma^{(i)}_{j\sigma}(i\omega_n)$ is for the Bethe lattice analogous to the substitution in equation (15) for Bravais lattices. Even for the Bethe lattice, the statDMFT involves therefore two approximations: the truncation of the effective single-site action and the conflation of the interaction self-energies (reminiscent of the substitution in equation (15) for Bravais lattices).

2.4. *Localization criterion*

A natural measure of the itinerancy suggested by the effective single-site action $S(i)$ is the total tunnelling rate from a given site i defined by the imaginary part of the hybridization function, $\Gamma_{i\sigma}(\omega) = J^2 \sum_{j \, \mathrm{NN} \, i} N^{(i)}_{j\sigma}(\omega)$, where $N^{(i)}_{j\sigma}(\omega)$ is the local cavity density of states (LCDOS), that is the imaginary part of the cavity Green function $G^{(i)}_{j\sigma j\sigma}(\omega)$. Obviously, a finite tunnelling rate $\Gamma_{i\sigma}(\omega)$ implies an extended state at energy ω. Localized states, in contrast, lead to a vanishing tunnelling rate. The tunnelling rate vanishes if the LCDOS $N^{(i)}_{j\sigma}(\omega)$ vanishes, which, in this sense, is a transport quantity and could by itself be used as a kind of 'order parameter' for localization. The tunnelling rate $\Gamma_{i\sigma}(\omega)$ as well as the LCDOS $N^{(i)}_{j\sigma}(\omega)$ are random variables and whether they vanish or not depends on their distribution. The shape of the distributions therefore has to change dramatically at the localization transition.

To understand why the shape of the distribution has to change, it is convenient to look at the distribution of a related quantity, the local density of states (LDOS), defined by

$$N_{i\sigma}(\omega) = -\frac{1}{\pi} \, \text{Im} \, [G_{i\sigma i\sigma}(\omega)], \tag{22}$$

because it directly reflects the spatial dependence of the wave function. For an extended state at energy ω, where the weights of the wave functions are more or less the same on every site, the distribution of the LDOS at energy ω is symmetric and the most probable value coincides with the arithmetic mean value (average value). Localized states with energy ω, on the other hand, have substantial weight only on a few sites. The distribution is therefore extremely asymmetric, with a most probable value much smaller than the arithmetic mean value, which is therefore not representative any longer. Since the LDOS $N_{j\sigma}(\omega)$ is closely related to the LCDOS $N_{j\sigma}^{(i)}(\omega)$, the distributions for the LCDOS and the tunnelling rate undergo the same characteristic change at the localization transition as the distribution for the LDOS.

A priori it is not clear by what moment (or moments) the asymmetric distributions should be characterized. At this point it is useful to anticipate that distributions and, in particular, the distribution for the local hybridization function can be used to calculate averaged transport quantities, such as the dc conductivity or the return probability (see below). The most probable value, that is the maximum of the distribution, is then expected to play a crucial role. (Note that averaged four-point functions (transport quantities) capture the localization effect, in contrast with averaged two-point functions.) It would therefore be natural to focus on the most probable values. The drawback is, however, that they cannot be directly obtained from the random samples; they require the explicit construction of histograms. More convenient quantities seem to be the so-called typical values (Dobrosavljević and Kotliar 1997, 1998), which are simply the geometric mean values of the random samples and yet capture the asymmetry of the distributions reasonably well. Therefore, we focus in this paper on the typical values.

In particular, we consider the distribution of the LDOS and distinguish localized from extended states by a detailed investigation of the average LDOS

$$N_\sigma^{\text{ave}}(\omega) = \frac{1}{N_\text{s}} \sum_i N_{i\sigma}(\omega), \tag{23}$$

and the typical LDOS

$$N_\sigma^{\text{typ}}(\omega) = \exp\left(\frac{1}{N_\text{s}} \sum_i \log\,[N_{i\sigma}(\omega)]\right). \tag{24}$$

Specifically, we classify states at energy ω with $N_\sigma^{\text{ave}}(\omega) \neq 0$ as localized if $N_\sigma^{\text{typ}}(\omega) \to 0$ and as extended if $N_\sigma^{\text{typ}}(\omega) \neq 0$. Note that the LDOS is defined for real energies. The numerical solution has to take this into account (see below). It should be stressed, Mirlin and Fyodorov (1994) also used the LDOS as an order parameter for the Anderson transition.

§3. Numerical results

3.1. *Statistical dynamic mean-field theory equations for a single electron*

This section presents a detailed numerical investigation of a single electron in the AHM at zero temperature. We solve the statDMFT equations for a Bethe lattice where, as mentioned in the previous section, the numerical effort is manageable. As in other areas of statistical physics, the Bethe lattice calculation has the status of a mean-field calculation for Bravais lattices. We expect therefore our results to be qualitatively valid for any Bravais lattice with $d \geqslant 3$.

The easiest way to obtain the zero-temperature single-particle limit of the statDMFT equations (equations (10)–(16)) is to work with an effective single-site Hamiltonian, instead of an effective single-site action. Neglecting the spin, which for a single electron is irrelevant, the effective Hamiltonian is

$$H(j)^{(i)} = \epsilon_j\, c_j^\dagger\, c_j + \Omega\, b_j^\dagger\, b_j - (E_\mathrm{p}\Omega)^{1/2}(b_j^\dagger + b_j)c_j^\dagger\, c_j$$
$$+ \sum_\nu E_\nu\, a_\nu^\dagger\, a_\nu + \sum_\nu (T_{\nu j}\, a_\nu^\dagger\, c_j + \mathrm{H.c.}), \tag{25}$$

where the notation indicates that the Hamiltonian models the dynamics encoded in the cavity effective single-site action $S(j)^{(i)}$.

The Hamiltonian representation of $S(j)^{(i)}$ is not unique. In equation (25) the embedding is given by the hybridization with an auxiliary field described by the operator a_ν. The auxiliary parameters E_ν and $T_{\nu j}$ have no physical meaning; they just parametrize the hybridization function in terms of a spectral representation:

$$H_{jj}(\mathrm{i}\omega_n) = \sum_\nu \frac{|T_\nu|^2}{\mathrm{i}\omega_n - \mu - \epsilon_j - E_\nu}. \tag{26}$$

For a given set of parameters $\{E_\nu, T_{\nu j}\}$, that is hybridization function $H_{jj}(\mathrm{i}\omega_n)$, the local self-energy $\Sigma_i(\mathrm{i}\omega_n)$ due to electron–phonon coupling can be deduced from equation (25). For finite densities, this can be done only by some approximation, introducing further uncertainties into the approach. For a single electron, however, the interaction self-energy can be obtained exactly in the form of a continued fraction (Sumi 1974, Ciuchi *et al.* 1997), valid over the whole range of parameters. Thus, for a single electron, no further approximations are required.

To be more specific, we calculate from equation (25) the single-electron Green function for $T = 0$, using the continued-fraction expansion for the electron–phonon self-energy, and identify then this Green function with the zero-temperature single-electron limit of the cavity Green function in equation (20). Setting $\mathrm{i}\omega_n + \mu \to z = \omega + \mathrm{i}\eta$, we obtain

$$G_{ii}^{(j)}(z) = \frac{1}{[F_{ii}(z)]^{-1} - \Omega E_\mathrm{p}/\big([F_{ii}(z-1\Omega)]^{-1} - 2\Omega E_\mathrm{p}/\{[F_{ii}(z-2\Omega)]^{-1} - 3\Omega E_\mathrm{p}/\ldots\}\big)} \tag{27}$$

with

$$F_{ii}(z) = \left(z - \epsilon_i - J^2 \sum_j G_{jj}^{(i)}(z) \right)^{-1}. \tag{28}$$

The local Green function follows from equation (21), setting again $i\omega_n + \mu \to z = \omega + i\eta$,

$$G_{ii}(z) = \frac{1}{[G_{ii}^{(j)}(z)]^{-1} - J^2 G_{jj}^{(i)}(z)}. \tag{29}$$

According to the interpretation given in the previous section, equations (27)–(29) constitute stochastic recursion relations for a random sample for the local Green function $G_\sigma^{\mathrm{loc}}(z)$. Note that Green functions with shifted energy appear in the continued fraction. They satisfy the same recursion relations, with energy shifted to $z - q\Omega$.

For a fixed energy $z - q\Omega$, the local Green functions $G_{ii}(z - q\Omega)$ are identically distributed. They are, however, not independent. As a consequence, for each energy $z - q\Omega$, we have to construct a separate random sample $\{G_{jj}^{(i)}(z - q\Omega)\}$ (with $j = 1, ..., N_s$ and $q = 0, 1, ..., M$, where N_s and M are the sample size and the maximum depth of the continued fraction, respectively), starting from an initial sample, which we successively update via a Monte Carlo algorithm, similar to the schemes described by other workers (Abou-Chacra *et al.* 1973, Girvin and Jonson 1980), drawing the random variables on the right-hand side of equation (27) from the corresponding random samples created by the iteration step before. Iterating this process a sufficient number of times yields, as a fixed point of the stochastic recursion relations, a self-consistent random sample for the cavity Green function at energy $z - q\Omega$. The self-consistent random samples are then used directly to determine average and typical values of the respective random variables or, in the form of histograms, the distributions associated with them.

For reasonable numerical accuracy, the sample size N_s, which should not be confused with the actual size of the Bethe lattice but instead gives the precision with which we construct the random sample (cf. distributions), has to be sufficiently large. Typical sample sizes are $N_s \approx 50\,000$. The maximum depth M of the continued fraction, which describes the maximum number of virtual phonons in the lattice, has to be large enough in order to capture polaron formation. As a rough estimate we use $M \approx 5g^2$, where $g^2 = E_p/\Omega$ is approximately the average number of virtual phonons in the phonon cloud of the polaron.

To distinguish localized from extended states, it is crucial to investigate the stochastic recursion relations in the limit $\eta \to 0$ (Abou-Chacra *et al.* 1973). Numerically this seems delicate. However, initializing the iteration loop with a finite imaginary part of the cavity Green functions, the stochastic recursion relations can be iterated without problems for $\eta = 0$ (Alvermann 2003). The correct self-consistent value of the imaginary part of the cavity Green function is then realized during the iteration.

Tracking random samples as a function of the iteration index provides therefore information about the character of the states at the energy for which the sample is constructed. Random samples corresponding to extended states converge rapidly to its fixed point, whereas random samples corresponding to localized states do not converge. Hence, extended and localized states can be detected by the differences that they give rise to in the mathematical properties of the recursion relations.

Sometimes it is advantageous to keep η finite, but then it is necessary to monitor the flow of the random samples, or of its associated average and typical values, as η becomes smaller and smaller. The part of the spectrum corresponding to extended states is insensitive to the η scaling; when η is small enough to see the correct LDOS, nothing changes any longer. Localized states on the other hand are strongly affected. In fact, it can be numerically verified that the typical LDOS indeed scales to zero with $\eta \to 0$ (Miller and Derrida 1993, Alvermann 2003).

To investigate the localization properties of electron and polaron states, we specifically focused on the typical LDOS, tracking this quantity, for given energy and model parameters, as a function of η and the number of iterations. Introducing a rescaled transfer amplitude $J = \bar{J}/\sqrt{K}$, we measure energies in units of the bare bandwidth $W_0 = 4\bar{J} = 1$ and define $\bar{\lambda} = E_p/2\bar{J}$, $\bar{\alpha} = \Omega/\bar{J}$ and $\bar{\gamma} = \gamma/4\bar{J}$. All calculations, except in appendix A, are carried out for the $K = 2$ Bethe lattice.

3.2. *Electron states*

To demonstrate the feasibility of the statDMFT and the associated localization criterion, we first discuss the localization properties of a single electron without coupling to phonons. In §3.3, we shall then contrast this well-understood situation with the results for the coupled electron–phonon system. Some of the results of this section are taken from Alvermann (2003).

We begin with a qualitative discussion of the distribution for the LDOS at $\omega = 0$, shown in figure 2 for $\bar{\gamma} = 0.2, 0.5, 1.0$ and 1.5 (inset). The shape of the distribution changes dramatically with increasing disorder: For small disorder ($\bar{\gamma} < 1$), the distribution is approximately a Gaussian. The most probable value and the average value almost coincide and change little with disorder (table 1). Thus, the main effect of small disorder is to broaden the distribution. For larger disorder ($\bar{\gamma} \geqslant 1$), on the other hand, the distribution develops a long tail, where
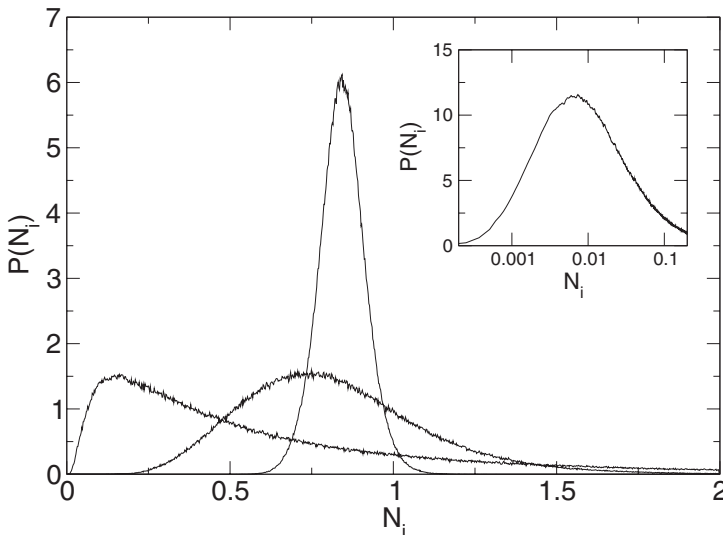

Figure 2.   Distribution for the LDOS at $\omega = 0$ for $\bar{\gamma} = 0.2, 0.5$ and 1.0. The inset shows the distribution for $\bar{\gamma} = 1.5$ on a logarithmic scale. In all cases, $\eta = 10^{-10}$.

Table 1. Average, most probable and typical LDOSs at $\omega=0$ corresponding to the distributions shown in figure 2.

$\bar{\gamma}$	N^{ave}	N^{mpv}	N^{typ}
0.2	0.844	0.843	0.841
0.5	0.822	0.749	0.773
1.0	0.710	0.162	0.445
1.5	0.568	0.006	0.106

the most probable value is now significantly smaller than the average value (see again table 1). For even larger disorder, close to the localization transition (for instance, for $\bar{\gamma} = 1.5$ shown in the inset of figure 2), the distribution becomes almost log-normal (Montroll and Shlesinger 1983). The average LDOS is now completely meaningless. Obviously, disorder not only broadens the distribution but also induces, if sufficiently strong, a change in the nature of the distribution.

From physical considerations, it is clear that the distribution of the LDOS for a fixed energy depends strongly on whether the states at that energy are extended or localized. The amplitude of an extended state is uniformly distributed over the whole system. Thus, the LDOS does not fluctuate much from site to site, that is the distribution of the LDOS at a given energy has to be centred around an average LDOS. On the other hand, the amplitude of a localized state is essentially zero everywhere, except in a small range around a central site. For a given energy there is a certain number of degenerate localized states, each centred at a different site. The LDOS fluctuates therefore strongly throughout the lattice. Accordingly, the distribution of the LDOS, for a given energy, has to be very broad, with a long tail, owing to the few sites where localized states have a large weight. Naturally, a complete characterization of the LDOS has to take the changes in the distribution into account, especially near the localization transition.

Within the statDMFT, distributions are represented by random samples. Any moment of the distribution, as well as the most probable value can be obtained from the histogram associated with the random sample. As indicated in §2.4, in practice it is often better to avoid the construction of the histogram and to characterize, instead, physical quantities by their typical values, which are simply the geometric averages of the random samples. From table 1 we see that the typical values capture the characteristic asymmetry of the distribution in the localized regime reasonably well ($N^{\mathrm{typ}} \ll N^{\mathrm{ave}}$ for $\bar{\gamma} > 1$). It is therefore indeed meaningful to use the typical LDOS as a kind of order parameter.

Let us now turn to a quantitative analysis of our results. In figure 3 we depict, for $\bar{\gamma} = 1.5$, the typical and average LDOSs over the whole spectral range of the pure Anderson model. The two main effects of disorder, the appearance of Lifshitz tails below $\omega = \pm 1.0$ and the existence of mobility edges around $\omega \approx \pm 0.8$, characterized by a vanishing of the typical LDOS (recall §2.4), can be clearly seen. The data have been obtained for $\eta = 10^{-10}$, which is sufficiently small to reveal the intrinsic spectrum and to allow a first estimate of the mobility edge.

A precise quantitative determination of the position of the mobility edge requires a calculation of the typical LDOS for $\eta \to 0$. We specifically consider the lower mobility edge. With the obvious modifications all statements also hold for the upper mobility edge.

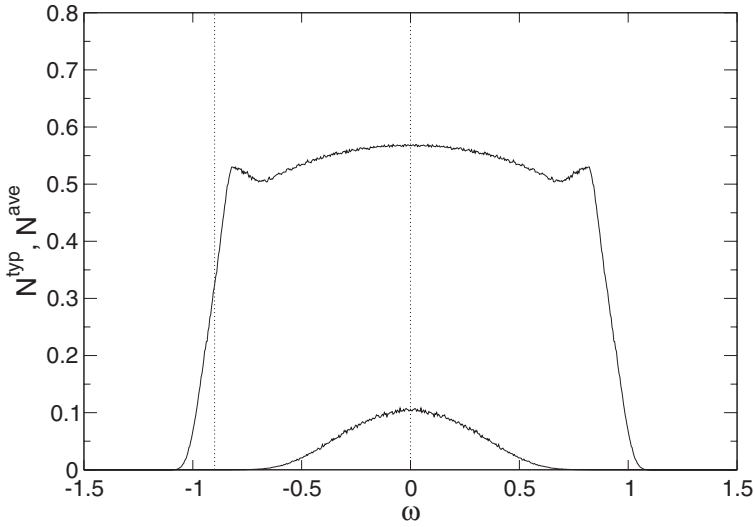Figure 3.   Average LDOS (upper curve) and typical LDOS (lower curve) for $\bar{\gamma} = 1.5$ and $\eta = 10^{-10}$. The vertical dotted lines indicate two energies, one below and the other above the lower mobility edge.
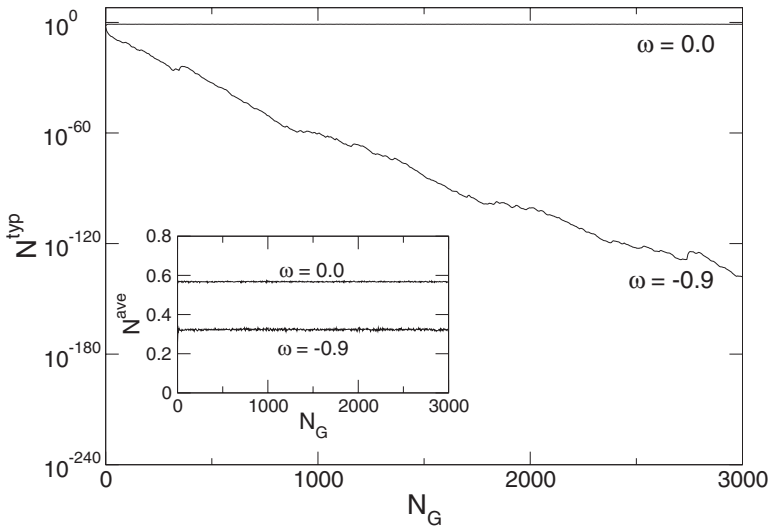

Figure 4.   Typical and average LDOSs below ($\omega = -0.9$) and above ($\omega = 0$) the lower mobility edge for $\bar{\gamma} = 1.5$ and $\eta = 0$ as functions of sample generation.

   To perform the $\eta \to 0$ limit numerically, we initialize the sample with a finite LDOS and then iterate the stochastic recursion relations for $\eta = 0$ until convergence. The iteration process yields the correct self-consistent LDOS. This procedure works extremely well, as can be seen in figure 4, where we plot the typical and average

LDOSs as functions of the iteration step (in other words, the sample generation) for $\bar{\gamma} = 1.5$, $\eta = 0$ and two energies (one below the lower mobility edge ($\omega = -0.9$) and the other above ($\omega = 0$)). As expected, below the lower mobility edge, the self-consistent value of the typical LDOS continues to decrease with increasing sample generation whereas, above the mobility edge, the typical LDOS remains finite. Note that, in both cases, the average LDOS stays finite and is essentially independent of the sample generation. This is the key observation; below (above) the lower mobility edge, the typical LDOS vanishes (stays finite), whereas the average LDOS remains finite in both cases.

At this point we should mention that the stable calculation of the average LDOS is subtle, because of the pure statistics associated with the long tail, which, on the other hand, determine the average value. To overcome this problem, we calculated the average LDOS after each iteration step and then performed an arithmetic average over the obtained values of the average LDOS. Since the typical number of iterations is $N_G \approx 1000$, we thereby effectively enlarged the sample size by three orders of magnitude, which was sufficient to obtain smooth data for the average LDOS (Alvermann 2003).

Thus, the tracking of the typical LDOS as a function of the sample generation can be utilized to decide whether states for a given energy are localized or not. In practice, one would screen all energies in the spectrum and set a small threshold for the typical LDOS, for instance 10^{-30}, below which the typical LDOS is assumed to be *de facto* zero. According to our localization criterion, states at that energy are then classified as localized. Since this procedure can be performed arbitrarily close to the mobility edge, the position of the mobility edge can be determined very precisely. It should also be mentioned that values for the typical LDOS of the order of 10^{-200} are not numerical artefacts. The small values are correctly captured by the floating-point representation of the typical LDOS.

An alternative is to use finite values of η and to track the typical LDOS with decreasing η. Below the lower mobility edge, the typical LDOS converges after a sufficient number of iterations to a value whose scale is set by the chosen η value whereas, above the lower mobility edge, the typical LDOS reaches an intrinsic value, completely unrelated to η. The average LDOSs are in both cases again finite. For this procedure to work, η has to be of course small enough to resolve the intrinsic spectrum. For instance, η should not mimic Lifshitz tails.

That the procedure based on the η dependence works excellently can be verified in figure 5. To clarify the origin of the differences in the η scaling of the typical and average LDOS below and above the lower mobility edge, we first look at the distributions. Below the lower mobility edge at $\omega = -0.9$, shown in figure 5(a), the distribution changes radically with decreasing η (note the logarithmic scale). The maximum of the distribution, that is the most probable value, shifts to very small values. In fact, η sets the scale for the most probable value. Accordingly, the typical value shown in the inset decreases with increasing η. Note, however, that the average value stays at a constant value, independent of η. Clearly, the average value is determined by the long tail, that is the few sites, where the localized wave functions have appreciable weight. The average LDOS is therefore extremely less probable and indeed not a representative value. In contrast, above the lower mobility edge at $\omega = 0$, shown in figure 5(b), the distribution is essentially independent of η. Accordingly, the typical as well as the average LDOSs do not change with η.
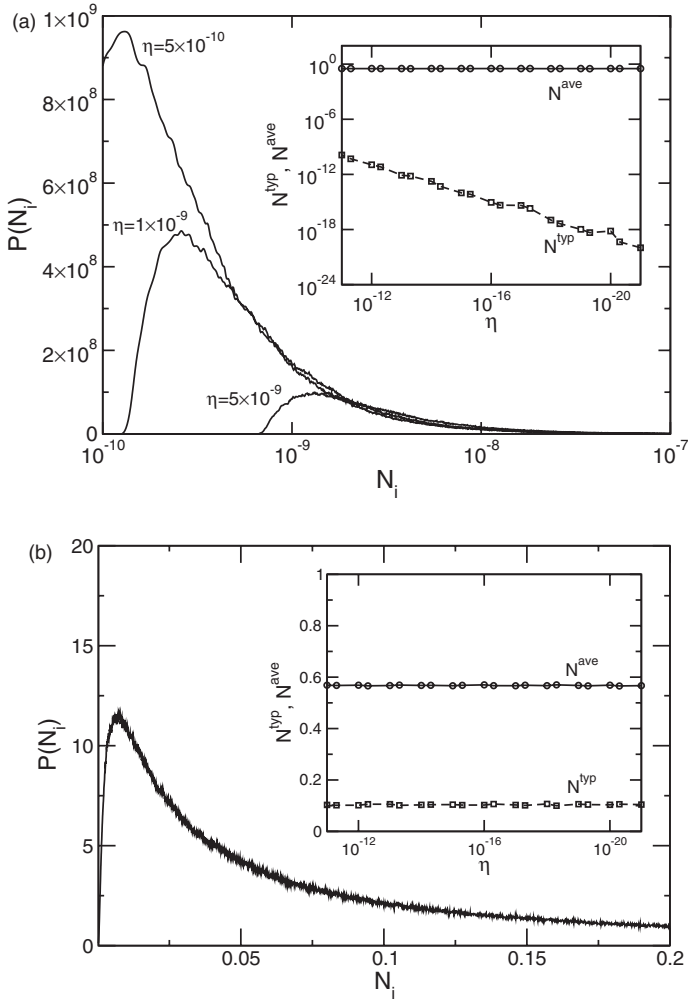
Figure 5.   The η scaling of the distribution for the LDOSs (*a*) below ($\omega = -0.9$) and (*b*) above ($\omega = 0$) the lower mobility edge for $\bar{\gamma} = 1.5$. In the insets we display the corresponding average and typical LDOSs as functions of η.

Below the mobility edge, the distributions for the LDOS, the LCDOS and the tunnelling rate $\Gamma^{\text{loc}}(\omega)$ become singular for $\eta \to 0$. This behaviour is closely connected with the configuration-averaged, spectrally resolved return probability

$$f_{ii}(\omega) = \lim_{\eta \to 0} \left(\frac{\eta}{\pi} \langle |G_{ii}(\omega + i\eta)|^2 \rangle_{\{\epsilon_i\}} \right), \tag{30}$$

which is finite for localized states and zero for extended states. To reveal this relationship, we follow the work of Logan and Wolynes (1987) and introduce a joint distribution for the real and imaginary parts of the local hybridization function $P(R(\omega), \Gamma(\omega))$ with $R(\omega) = \text{Re}\,[H^{\text{loc}}(\omega)]$ and $\Gamma(\omega) = \text{Im}\,[H^{\text{loc}}(\omega)]$, in terms of which we obtain

$$f_{ii}(\omega) = \lim_{\eta \to 0} \left(\int_0^\infty \mathrm{d}\Gamma(\omega) \, \frac{D(\omega, \Gamma(\omega))}{1 + \eta^{-1}\Gamma(\omega)} \right), \tag{31}$$

with

$$D(\omega, \Gamma(\omega)) = \frac{1}{\pi} \int_{-\infty}^\infty \mathrm{d}\epsilon \int_{-\infty}^\infty \mathrm{d}R(\omega) \, \frac{[\eta + \Gamma(\omega)] \, p(\epsilon) P(R(\omega), \Gamma(\omega))}{[\omega - \epsilon - R(\omega)]^2 + [\eta + \Gamma(\omega)]^2}. \tag{32}$$

If the state at energy ω is localized, the (marginal) distribution for $\Gamma(\omega)$, that is $P(\Gamma(\omega)) = \int_{-\infty}^\infty \mathrm{d}R(\omega) \, P(R(\omega), \Gamma(\omega))$, is strongly peaked around $\Gamma^{\mathrm{mpv}}(\omega) \to 0$ (cf. figure 5). In that regime, $D(\omega, \Gamma(\omega)) \approx \delta[\Gamma(\omega) - \Gamma^{\mathrm{mpv}}(\omega)] N^{\mathrm{cav}}(\omega)$, with $N^{\mathrm{cav}}(\omega) = -(1/\pi) \, \mathrm{Im}\,[G_{jj}^{(i)}(\omega)]$ denoting the LCDOS (Logan and Wolynes 1987). Accordingly, equation (31) reduces to

$$f_{ii}(\omega) = \lim_{\eta \to 0} \left(\frac{N^{\mathrm{cav}}(\omega)}{1 + \eta^{-1}\Gamma^{\mathrm{mpv}}(\omega)} \right), \tag{33}$$

which, provided that $N^{\mathrm{cav}}(\omega) \neq 0$, is finite, because $1 + \eta^{-1}\Gamma^{\mathrm{mpv}}(\omega) \to 2$ for $\eta \to 0$. In other words, the singular behaviour of the distribution for $\Gamma^{\mathrm{loc}}(\omega)$ gives rise to a pole in $\langle |G_{ii}(\omega + \mathrm{i}\eta)|^2 \rangle_{\{\epsilon_i\}}$ which in turn makes $f_{ii}(\omega)$ finite. From diagrammatic approaches it is known that maximally crossed diagrams, responsible for destructive interference, produce a pole in $\langle |G_{ii}(\omega + \mathrm{i}\eta)|^2 \rangle_{\{\epsilon_i\}}$. Equation (31) provides therefore a link between the interference-based description of Anderson localization and the probabilistic approach adopted by the statDMFT.

The η scaling discussed in figure 5 can be followed all the way down to $\eta = 0$, suggesting a precise procedure for the determination of mobility edges. In practice, however, we cut off the scaling at a certain threshold, for instance 10^{-30}. If the typical LDOS for a given energy ω is below the threshold, and if for that energy the average LDOS is finite, we classify the state at energy ω as localized. For $\omega = 0$ this is shown in figure 6. Clearly, for $\omega = 0$ the typical LDOS tends to zero for $\bar{\gamma} \approx 2.9$. The average LDOS on the other hand is independent of η and remains finite. Thus, according to our localization criterion, the state at energy $\omega = 0$ is localized for $\bar{\gamma} \geqslant 2.9$, in accordance with results obtained by Girvin and Jonson (1980) and by Miller and Derrida (1993).

Performing the analysis for all energies in the spectrum, we can systematically map out the mobility edge trajectory. The result is shown in figure 7. Note that the statDMFT is accurate enough to detect the two transitions associated with the characteristic re-entrant behaviour of the mobility edge trajectory near the band edge: the delocalization transition at small disorder and the localization transition at large disorder. Even in the strongly disordered regime, where the mobility edges move to the centre of the band and all states are localized, the statDMFT works reliably well. We did not attempt to estimate the statistical error, but it should be of the order of the fluctuations visible in the plot.

Our results are in excellent agreement with results obtained by Miller and Derrida (1993), suggesting that, within the statDMFT, mobility edges for non-interacting electrons can be indeed determined. In §3.3, we shall demonstrate, that the statDMFT is flexible and powerful enough to determine mobility edges in interacting systems as well.
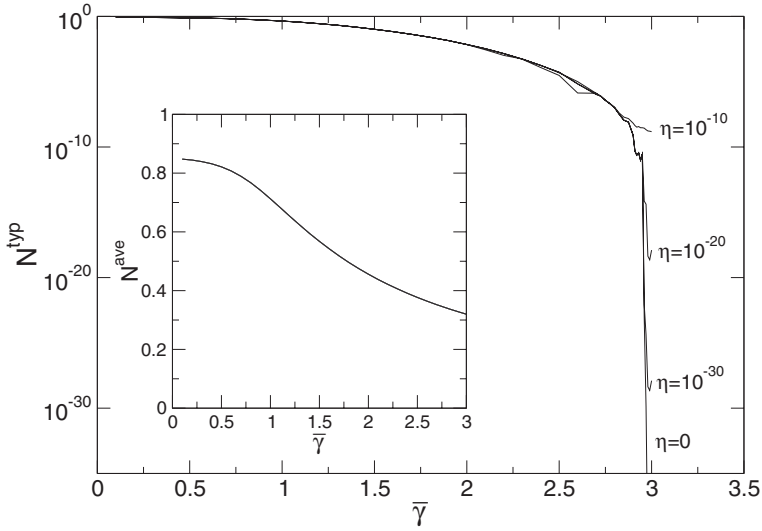
Figure 6.   The η scaling of the typical and average (inset) LDOSs at $\omega = 0$ for $\bar{\gamma} = 1.5$. Note that, for the chosen η values, the average LDOS is independent of η.
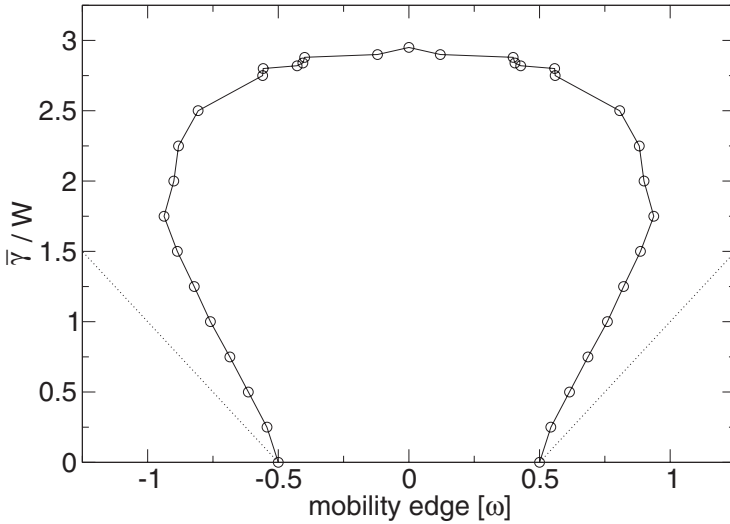

Figure 7.   Mobility edge trajectory for an electron in the pure Anderson model. The dotted lines indicate the position of the band edges defined by $\pm (W/2 + \gamma/2)$.

3.3. *Polaron states*

We now turn our attention to the consequences of the electron–phonon coupling. If the electron–phonon coupling is weak, the main effect is that the electron states above the phonon emission threshold, that is states whose kinetic energy is at least the phonon energy Ω, acquire a finite lifetime owing to inelastic scattering, which gives rise to $\mathrm{Im}[\Sigma_i(\omega)] \neq 0$. As a result, the critical disorder needed to localize these states will be larger than without electron–phonon coupling. For the states below the phonon emission threshold, we have $\mathrm{Im}[\Sigma_i(\omega)] = 0$, and the critical dis-

order is the same as for the respective states in the pure Anderson model (Bronold and Fehske 2002).

Increasing the electron–phonon coupling to the point where $\bar{\lambda} > 1/(K)^{1/2}$ and $g^2 > 1$, polaron formation starts and the LDOS fragments into an increasing number of polaronic subbands (Sumi 1974, Ciuchi *et al.* 1997). The lowest subbands are either completely or partly coherent, that is $\mathrm{Im}\,[\Sigma_i(\omega)] = 0$, whereas the higher-order subbands are strongly damped because $\mathrm{Im}\,[\Sigma_i(\omega)] \neq 0$. Thus, in the polaron regime, we have two energy scales: the bare bandwidth and the much smaller width of the polaronic subbands. Obviously, the width of the distribution of the on-site energies ϵ_i can be small on the scale of the bare bandwidth but large on the scale of the subband. We distinguish therefore between two regimes: the Holstein regime, where disorder is small on the scale of the bare bandwidth, and the Anderson regime, where it is large on the scale of the width of the subband.

3.3.1. *Holstein regime*

For our purpose the lowest polaronic subband is of particular interest, because it is always completely coherent, that is $\mathrm{Im}\,[\Sigma_i(\omega)] = 0$ throughout the subband, and no inelastic polaron–phonon scattering interferes with the localization properties of the polaron.

First, we consider the *anti-adiabatic strong-coupling* regime, where the phonon admixture of the states constituting the lowest polaronic subband is almost energy independent. Phonon-induced long-range tunnelling as well as band flattening (Stephan 1996, Fehske *et al.* 1997a) are absent and the LDOS without disorder is rather symmetric. Numerical simulations (Stephan 1996, Fehske *et al.* 1997a) of the Holstein model indicate that the lowest subband in that case is just a rescaled bare band. Accordingly, we expect disorder to affect the polaronic subband in the same way as it affects the band of the pure Anderson model. Most notably, the mobility edges should simultaneously appear on both sides of the subband. Furthermore, the mobility edge trajectories should show the characteristic re-entrant behaviour at the band edges and the critical disorder needed to localize all states of the subband should be determined by the states in the centre of the subband. In fact, with an appropriate scaling, the mobility edge trajectories for the lowest polaronic subband and the pure Anderson model should coincide. We now demonstrate that this is indeed the case.

We start with figure 8, which shows, for $\bar{\alpha} = 2.25$ and $\bar{\lambda} = 9$, the average and typical LDOSs for the lowest subband; $\bar{\gamma} = 2.5\,W$ with $W = 3.45 \times 10^{-4}$ the width of the subband in units of $W_0 = 4\bar{J}$. For comparison, we also show the DMFT result for the LDOS. As expected, the average LDOS is rather symmetric, the small asymmetry reflecting the fact that we are not yet in the extreme anti-adiabatic regime. As far as the effect of disorder is concerned, we see the same overall features as in the pure Anderson model (cf. figure 3): the appearance of Lifshitz tails and of mobility edges. The typical LDOS, shown in figure 8 for $\eta = 10^{-8}$ and $\eta = 10^{-14}$, vanishes on both sides of the subband, clearly indicating the existence of mobility edges on both sides of the subband. As discussed before, a precise determination of the position of the mobility edges requires us either to calculate the typical LDOS for $\eta = 0$ and to track the iteration flow with sample generation, or to follow the η scaling of the LDOS.

For a quantitative calculation of the mobility edges, we adopted here the η scaling approach. In figure 9 we show, for the two representative energies indicated in
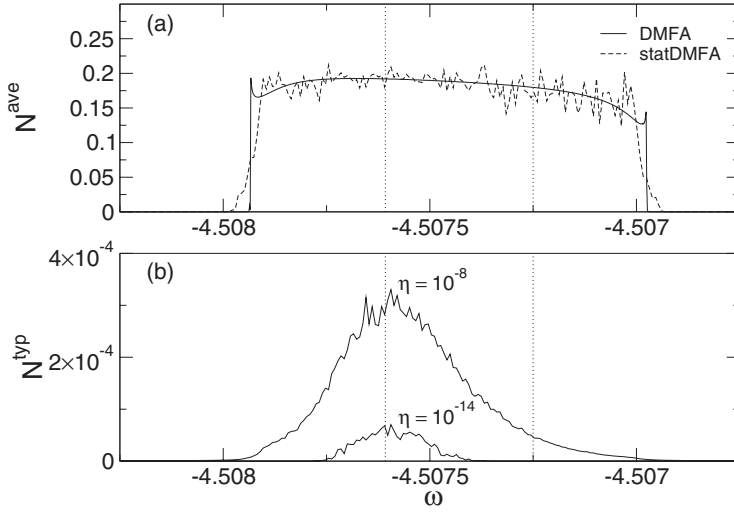
Figure 8. (*a*) Average and (*b*) typical LDOSs for the lowest polaronic subband in the anti-adiabatic strong-coupling regime for $\bar{\gamma} = 2.5 \times W$; $W = 3.45 \times 10^{-4}$ is the width of the lowest subband of the pure Holstein model in units of $W_0 = 4\bar{J} = 1$. The polaron parameters are $\bar{\alpha} = 2.25$ and $\bar{\lambda} = 9$. The vertical dotted lines indicate two energies, one above ($\omega = -4.507\,25$) and the other below ($\omega = -4.507\,59$) the upper mobility edge for the subband.

figure 8, the η scaling of the distribution for the typical LDOS, the typical LDOS and the average LDOS. Above the upper mobility edge at $\omega = -4.507\,25$, the distribution shows the characteristic properties associated with localized states: an extremely small most probable value and a long tail resulting in an average value much larger than the most probable value. The typical LDOS again scales to the fixed η value, while the average LDOS is independent of η. For the extended states at $\omega = -4.507\,59$, on the other hand, we again see that the distribution is insensitive to η and both average and typical LDOSs converge to finite values independent of η.

As for the pure Anderson model, tracking the η scaling of the LDOS for all energies in the subband enables us to map out the mobility edge trajectory for the subband. From physical considerations, we know that the trajectory should be the same as for the pure Anderson model. Instead of calculating the whole mobility edge trajectory, it is therefore sufficient to verify, for representative energies, that the two mobility edge trajectories indeed coincide.

As a first demonstration of this assertion, we plot in figure 10 the typical LDOS for $\omega = -4.507\,59$ (roughly the centre of the subband) scaled to its value at $\bar{\gamma} = 0$ as a function of disorder in units of the width of the subband and compare it with the scaled typical LDOS at $\omega = 0$ for the pure Anderson model, again as a function of $\bar{\gamma}$ scaled to the bandwidth. As anticipated, the two plots coincide. As in the pure Anderson model, the state at the centre of the (sub)band is localized for $\bar{\gamma}/W \geqslant 2.9$.

To provide further evidence for our assertion that the localization properties of the lowest subband in the anti-adiabatic strong-coupling regime are those of a rescaled Anderson model, we explicitly calculated for a few selected energies
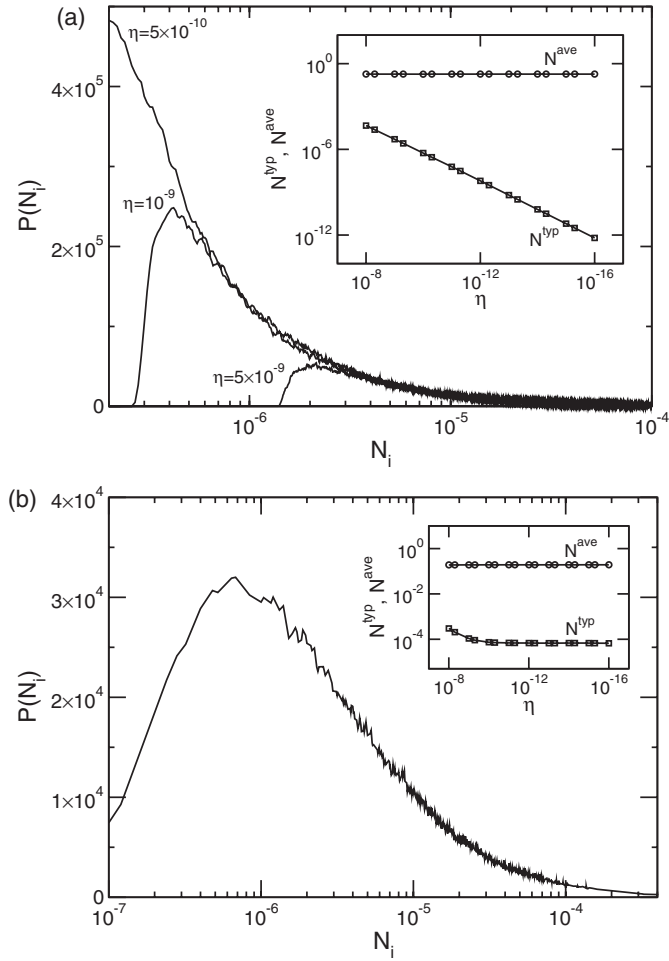
Figure 9. The η scaling of the distribution for the LDOS at the two energies indicated in figure 8: (a) $\omega = -4.507\,25$ (above the upper mobility edge); (b) $\omega = -4.507\,59$ (below the upper mobility edge). The insets show the corresponding average and typical LDOSs as functions of η.

the critical disorder needed to localize the states at these energies and, thereby, constructed parts of the mobility edge trajectory for the lowest subband. Note the extremely high precision of our approach, which enables us to determine the mobility edge trajectory of a subband whose width without disorder is 3.45×10^{-4} in units of $W_0 = 4\bar{J} = 1$. The results are shown in figure 11 (open circles). Obviously, the data points for the subband follow exactly the trajectory of the pure Anderson model, even at very strong disorder, where all states of the subband are localized (see data point at $\bar{\gamma}/W \approx 2.9$). In the anti-adiabatic strong-coupling regime, the localization behaviour of the states of the lowest subband is therefore identical with the behaviour of the states in a rescaled Anderson model. The polaron effect and, in particular, the band collapse only change the energy scale on which localization takes place; the internal structure of the polaron states does not affect the localization properties. Thus, in the anti-adiabatic strong-coupling regime, disorder
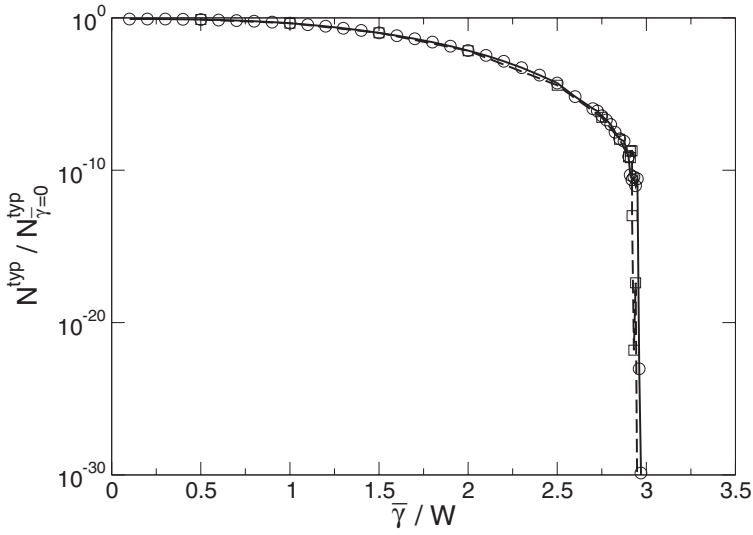
Figure 10. The typical LDOS (□) at the centre of the lowest subband of the Anderson–Holstein model (roughly at $\omega = -4.507\,59$) scaled to its value for $\bar{\gamma} = 0$ as a function of disorder measured in units of the width of the subband W; $\bar{\alpha} = 2.25$ and $\bar{\lambda} = 9$. For comparison, we also plot the scaled typical LDOS (○) at the centre of the band for the pure Anderson model as a function of the scaled disorder.
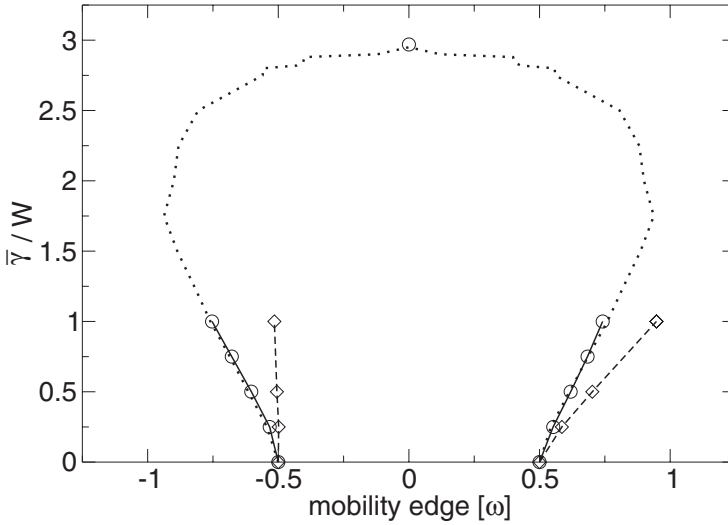

Figure 11. Parts of the mobility edge trajectories for the lowest polaronic subband of the AHM in the anti-adiabatic strong-coupling regime ($\bar{\alpha} = 2.25$ and $\bar{\lambda} = 9$) (○), and the adiabatic intermediate- to strong-coupling regime ($\bar{\alpha} = 0.2$ and $\bar{\lambda} = 1$) (◇) and the pure Anderson model (···). Disorder is measured in units of the respective width of the subbands, which, for the plot, are scaled to $W_0 = 4\bar{J} = 1$.

can be sufficiently strong to localize all states of the lowest subband and yet too small to interfere with the internal structure of the polaron.

   This is not the case in the *adiabatic intermediate- to strong-coupling regime*, where we find substantial differences between the localization properties of the
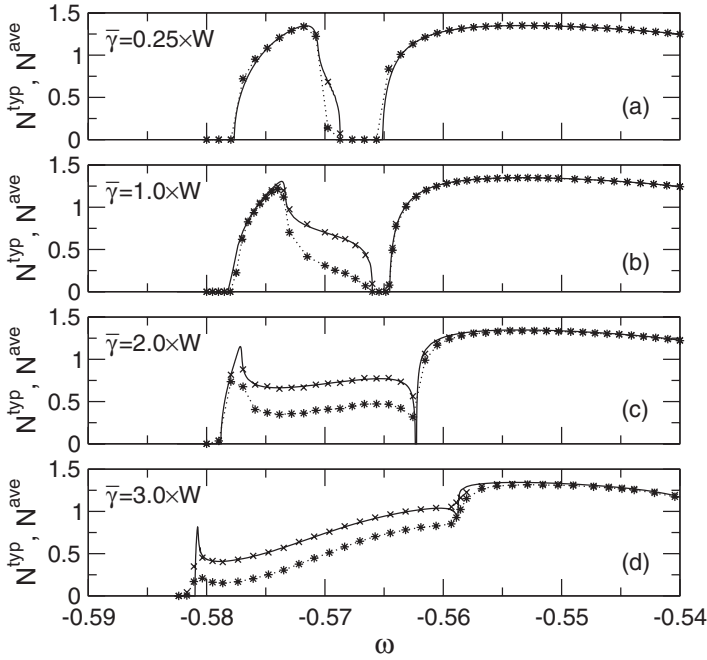
Figure 12. Average ($\times$) and typical ($\star$) LDOSs and the DMFA result (—) for the LCDOS for $\bar{\alpha} = 0.2$, $\bar{\lambda} = 1$ and four different values for the disorder strength: (*a*) $\bar{\gamma} = 0.25\,W$, (*b*) $\bar{\gamma} = 1\,W$, (*c*) $\bar{\gamma} = 2\,W$, and (*d*) $\bar{\gamma} = 3\,W$, with $W = 8.123 \times 10^{-3}$ is the width of the lowest polaron subband of the pure Holstein model (in units $W = 4\bar{J} = 1$).

lowest polaronic subband and the band of the pure Anderson model. The differences originate in the changing composite structure of the polaron states within the lowest subband. In particular, at the top of the subband, where the band flattening due to the hybridization with the optical phonon branch significantly modifies the LDOS, the localization properties deviate strongly from a rescaled pure Anderson model. However, also at the bottom of the subband, significant deviations can be observed because of the phonon-induced long-range tunnelling processes.

In figure 12 (*a*) we show, for $\bar{\alpha} = 0.2$, $\bar{\lambda} = 1$ and $\bar{\gamma} = 0.25 \times W$, the average and typical LDOSs for the lowest subband. Here, $W = 8.123 \times 10^{-3}$ is the width of the subband for the pure Holstein model (in units of $W_0 = 4\bar{J} = 1$). In contrast with the anti-adiabatic strong-coupling case, the LDOS is strongly asymmetric, a direct result of the band flattening which yields a peak at the top of the LDOS. States in the peak, belonging to the flat part of the dispersion, are already sluggish and therefore very susceptible to disorder. The typical LDOS vanishes therefore rapidly at the top of the subband. At the bottom, however, where states are rather mobile owing to phonon-induced long-range tunnelling and hence are less affected by disorder, the typical LDOS is finite.

To determine the position of the mobility edges we again employ the η-scaling approach. In figure 11 (open diamonds) we show for $\bar{\alpha} = 0.2$ and $\bar{\lambda} = 1$ parts of the mobility edge trajectory for the lowest subband in the adiabatic strong-coupling regime. As expected, the states at the bottom of the subband are almost insensitive to small amounts of disorder, resulting in a lower mobility edge which is pinned at

the lower band edge, which in fact also does not change. States at the top of the subband, in contrast, are immediately affected by disorder. Small amounts of disorder (small even on the scale of the subband) are sufficient to shift the upper band edge to higher energies and to localize the states at the top of the subband. The upper mobility edge moves very rapidly away from the upper band edge. As a result, the mobility edge trajectory for the lowest subband in the adiabatic strong-coupling regime is very asymmetric (for small disorder).

For large disorder (not shown in figure 11), of the order of the width of the subband, the upper band edge of the disorder-broadened lowest subband moves into a spectral range with significant inelastic scattering. The reason is the following. Without disorder, subbands are separated by singularities in the imaginary part of the electron–phonon self-energy. Increasing disorder redistributes states. In particular, it moves states into the gap region, which separated the first from the second subband, thereby giving rise to a shrinking gap. Concomitantly, the singularity in the electron–phonon self-energy broadens, and its state-repelling character weakens, resulting in an enhanced inelastic scattering rate for the states at the top of the lowest subband, which strongly suppresses localization in this spectral range. Both effects, the merging of the subbands and the increased inelastic scattering, occur before a re-entrant behaviour of the mobility edge trajectories can be observed.

To support the scenario just described we depict in figures 12 (*b*)–(*d*), for polaron parameters $\bar{\alpha} = 0.2$ and $\bar{\lambda} = 1$, the typical and average LDOSs for $\bar{\gamma} = 1\,W$, $2\,W$ and $3\,W$. Again, $W = 8.123 \times 10^{-3}$ is the width of the subband for the pure Holstein model (in units of $W_0 = 4\bar{J} = 1$). In figures 12 (*b*)–(*d*), all states of the lowest subband are now delocalized, and the typical LDOS is finite for all energies constituting the lowest subband. For figure 12 (*a*), where a small gap still separates the two lowest subbands, the asymmetric localization behaviour of the states at the bottom and the top of the lowest subband is still visible. Nevertheless, inelastic scattering is so strong as to make the typical LDOS finite even at the top of the subband. With increasing disorder, shown in figures 12 (*b*)–(*d*), the gap vanishes. More importantly, however, the typical LDOS increases with increasing disorder. Thus, in this regime, disorder delocalizes states. Eventually, of course, with disorder on the scale of the bare bandwidth, all states would be localized. However, the critical disorder strength is larger than in the case of the pure Anderson model, because the inelastic scattering has to be overcome.

The merging of the subbands signals that the internal structure of the polaron states and disorder start to interfere strongly with each other. With the vanishing subband structure, the concept of a subband mobility edge trajectory breaks down and a re-entrant behaviour of the mobility edge trajectory cannot be established.

3.3.2. *Anderson regime*

The vanishing subband structure characterizes a transition regime, between the Holstein and the Anderson regime, where disorder is on the scale of the energy gap between the subbands. The localization properties in the transition region are rather complicated and beyond the scope of this paper. The situation becomes more transparent in what we call the Anderson regime, where disorder is large compared with the width of the polaronic subbands.

In figure 13 we show the typical and average LDOSs, for $\bar{\alpha} = 0.2$, $\bar{\lambda} = 0.75$ and $\bar{\gamma} = 2$. Without electron–phonon coupling, there would be mobility edges at $\omega \approx \pm 0.9$. In the presence of electron–phonon coupling, we first note that the
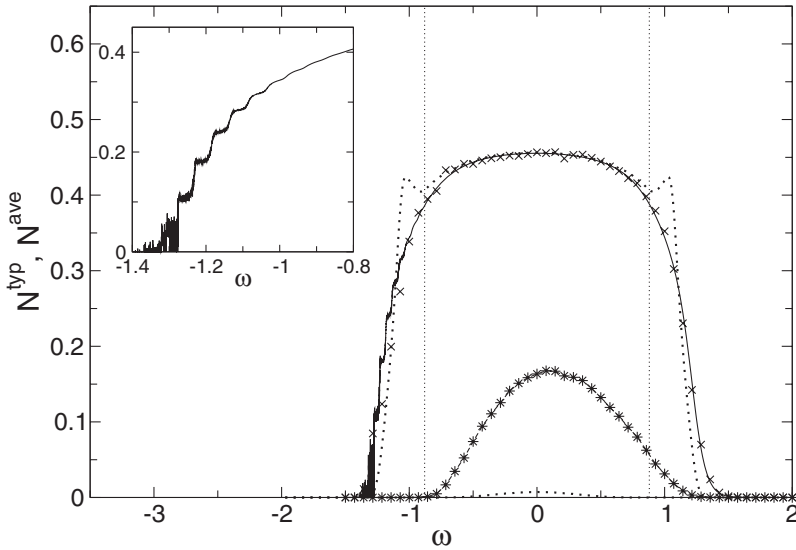
Figure 13. Average ($\times$) and typical LDOS ($\star$) in the Anderson regime for $\bar{\alpha} = 0.2$, $\bar{\lambda} = 0.75$ and $\bar{\gamma} = 2$: (—), the LCDOS obtained from DMFT (a magnification of the low-energy part is shown in the inset); ($\cdot \cdot \cdot$), the average and typical LDOSs for $\bar{\lambda} = 0$; the vertical dotted lines indicate the mobility edges of the non-interacting system.

symmetry between the lower and upper mobility edges is broken. The lower mobility edge is located at $\omega \approx -0.8$, which is above the mobility edge of the non-interacting system. (Here, we did not perform the η scaling necessary for a precise determination of the mobility edge.) Thus, at the low-energy edge, electron–phonon coupling enhances the tendency towards localization. The upper mobility edge, in contrast, is shifted to higher energies ($\omega \approx 1.2$); that is, at the upper band edge, electron–phonon coupling delocalizes states and works against localization. If we mapped out a mobility edge trajectory, we would find a pronounced asymmetry between the lower and the upper parts of the trajectory.

The asymmetry can be explained, if we recall that our calculation is for $T = 0$. Therefore, states at energy ω can, owing to electron–phonon interaction, only couple to states at energies less than ω. This leads on the high-energy side of the LDOS to a phonon-induced coupling of localized states above the mobility edge of the non-interacting system to delocalized states below. As a consequence, the localized states become delocalized. On the low-energy side, the situation is different. States below the lower mobility edge of the non-interacting system remain localized, because they can only couple to states that are already localized. Above the lower mobility edge of the non-interacting system, electron–phonon interaction attempts, however, to transform electronic band states into polaronic (sub)band states, as suggested by Anderson (1972). Hence, these states become heavier and more susceptible to disorder. As a consequence, the lower mobility edge of the interacting system shifts above the lower mobility edge of the non-interacting system.

Further insight about the nature of the states can be gained from the LCDOS obtained within the DMFT (see solid curves in figure 13 and inset). Because of electron–phonon coupling, the DMFT results for the LCDOS show on the low-

energy side pronounced plateaus with a width given by the phonon energy. (The spikes are numerical artefacts.) The step-like increase in the DMFT LCDOS, together with the vanishing of the typical LDOS, is a clear signature for localized polaron states. The character of the states is here revealed by the DMFT LCDOS. It arises from polaronic defects (cf. the independent boson model (Mahan 1990)), which are centred around different on-site energies, because of the disorder. Since they are decoupled, the DMFT LCDOS (with a higher resolution we would see the same in the average LDOS) does not change with energy as long as the fluctuations of the on-site energies are smaller than the phonon energy. If the difference in on-site energies is equal to the phonon energy, a step arises because states with one additional phonon contribute. The step heights reflect therefore the phonon distribution of the polaronic defect states.

Whereas, in the adiabatic intermediate- to strong-coupling regime, *disorder* affects states differently at the bottom and the top of the polaronic subband, in the Anderson regime, *electron–phonon coupling* affects states in the vicinity of the lower and upper mobility edges of the non-interacting system differently. Only in the vicinity of the lower mobility edge of the non-interacting system, do electron–phonon coupling and localization work in the same direction. At the upper mobility edge, electron–phonon coupling in fact delocalizes states.

§4. Conclusions

We have adopted the statDMFT for the AHM to develop a self-consistent theory of localization in a generic disordered electron–phonon system. In particular, we investigated the localization properties of a single electron over a wide range of polaron parameters (adiabaticity and electron–phonon coupling strength).

Our approach is non-perturbative in the electron–phonon coupling and accounts for the spatial fluctuations of the environment by promoting all variables of the theory to random variables. The object of the theory is to calculate distributions (random samples). Of particular importance are the distributions for the LDOS, the LCDOS and the tunnelling rate. Whereas information about the spatial dependence of the wave function Ψ_i can be extracted from the distribution for the LDOS, that is $\Psi_i \leftrightarrow P(N_i)$, the configuration-averaged, spectrally resolved return probability is closely related to the distributions for the LCDOS and the tunnelling rate, that is $f_{ii} \leftrightarrow P(N_i^{(j)}), P(\Gamma_i)$ (see equation (31)).

In this paper, we focused on the distribution for the LDOS. Since it is a measure of the spatial distribution of the wave function, it contains direct information about the localization properties; states are localized if the distribution of the LDOS is very asymmetric with an extremely long tail. Although the tail, which is due to the few sites on which (localized) wave functions are finite, makes the average LDOS finite, the more representative typical LDOS vanishes. Delocalized states, on the other hand, are characterized by a symmetric distribution of the LDOS for which the typical and average LDOSs are of the same order of magnitude.

Using the typical LDOS to distinguish localized from extended states, we investigated in detail the localization properties of a single electron in the AHM. We distinguished two parameter regimes. The weakly disordered Holstein regime, where disorder is small on the scale of the bare bandwidth and the polaronic subband structure is well developed, and the strongly disordered Anderson regime, with

disorder large on the scale of the width of the subband, strong enough to interfere with the internal structure of the polaron states.

In the weakly disordered Holstein regime, we focused on a comparison of the mobility edge trajectories for the lowest polaronic subband and the bare band of the Anderson model. We found significant deviations, most notably in the adiabatic, intermediate- to strong-coupling regime. Two main conclusions can be drawn from our studies: In the strong-coupling anti-adiabatic regime, the internal structure of the polaron is irrelevant and the localization properties of the lowest polaronic subband are essentially those of a rescaled Anderson model. The overall scale of the disorder is of course much smaller in the polaron case, suggesting that Holstein are most probably always localized at $T = 0$. The internal structure of the phonon dressing contributes the most in the adiabatic intermediate- to strong-coupling regime. Initially, for small disorder $\bar{\gamma} < W$ (W is the width of the lowest subband in the clean system), states at the high-energy edge of the lowest polaronic subband are extremely sensitive to disorder and rather easy to localize, whereas states at the bottom are almost insensitive to disorder. In contrast with the pure Anderson model, the mobility edge trajectory (in the disorder range where it can be defined) is not symmetric with respect to the band centre. Whereas the lower mobility edge is pinned to the lower band edge, the upper mobility edge moves quickly away from the upper band edge. Re-entrant behaviour of the upper mobility edge towards the centre of the subband cannot be observed because, at larger disorder strength, sub-bands vanish and the concept of a subband mobility edge trajectory obviously breaks down.

The merging of polaron subbands is characteristic for a transition regime where disorder is of the order of the energy gap and strongly interferes with the internal structure of the polaron states. Detailed investigation of this regime is beyond the scope of this paper. Instead we presented results for the Anderson regime, where disorder is much larger than the width of the subbands. In this regime disorder and electron–phonon coupling work in the same direction at the bottom of the band, where electron–phonon coupling even enhances the tendency towards localization, and against each other at the top, where electron–phonon coupling delocalizes states above the upper mobility edge of the non-interacting system. In the Anderson regime, the mobility edge trajectory would acquire therefore a pronounced asymmetry.

Several issues must, however, be clarified before real materials with polaronic excitations can be analysed along the lines presented in this paper. In most polaronic materials, electron densities are finite. The most pressing issue is therefore the consideration of the polaron–polaron interaction, mediated either by phonons or by the Coulomb potential of the electron charge. In principle, the statDMFT is capable of tackling this challenging problem. The main obstacle here is the controlled calculation of the interaction self-energy for the ensemble of impurity models. The exact continued-fraction expansion works only for a single electron and cannot be adapted to finite densities. For finite densities, the interaction self-energy has to be obtained by perturbation theory. To overcome the limitations of the perturbation theory, it is also conceivable to use direct numerical simulations of the ensemble of the local Green function, based, for instance, on quantum Monte Carlo or exact diagonalization techniques. The localization properties *per se* can again be simply extracted from an analysis of the distribution for the LDOS.

APPENDIX A

§A1. DYNAMIC MEAN-FIELD THEORY

For a lattice with infinite coordination number, the statDMFT reduces to the DMFT. To demonstrate this point, it is convenient to scale the transfer amplitude $J \to \bar{J}/(K)^{1/2}$ (Bronold and Fehske 2002).

Restricting for simplicity the discussion to the Bethe lattice, equation (21) shows that, for $K \to \infty$, cavity and local Green function are identical and equation (19) becomes

$$G_{i\sigma i\sigma}(\mathrm{i}\omega_n) = \frac{1}{\mathrm{i}\omega_n + \mu - \epsilon_i - \bar{J}^2 G_\sigma^{\mathrm{ave}}(\mathrm{i}\omega_n) - \Sigma_\sigma(\mathrm{i}\omega_n)}, \tag{A1}$$

where we have used the central limit theorem to replace the hybridization function on the right-hand side by the average of the local Green function. At this point the scaling of J is most convenient.

The self-energy is calculated from the effective single-site action $S(i)$ where, again owing to the central limit theorem, the hybridization function is replaced by $\bar{J}G_\sigma^{\mathrm{ave}}$. The self-energy is therefore a functional of $G_\sigma^{\mathrm{ave}}(\mathrm{i}\omega_n)$; that is, on the right-hand side of equation (A1) the only random variable is ϵ_i. The sample average $(1/K)\sum_{j=1}^{K}(...)$ of equation (A1) is therefore identical with the site average over ϵ_i. Denoting the site average by $\langle\ldots\rangle_{\epsilon_i}$, we obtain

$$G_\sigma^{\mathrm{ave}}(\mathrm{i}\omega_n) = \left\langle \left[\mathrm{i}\omega_n + \mu - \epsilon_i - \bar{J}^2 G_\sigma^{\mathrm{ave}}(\mathrm{i}\omega_n) - \Sigma_\sigma[\epsilon_i, G_\sigma^{\mathrm{ave}}]\right]^{-1} \right\rangle_{\epsilon_i}, \tag{A2}$$

which, together with

$$S(i)\Big|_{K\to\infty} = \int_0^\beta \mathrm{d}\tau\,\mathrm{d}\tau' \sum_\sigma c_{i\sigma}^\dagger(\tau)\left[(\partial_\tau + \epsilon_i - \mu)\delta(\tau - \tau') + \bar{J}^2 G_\sigma^{\mathrm{ave}}(\tau - \tau')\right] c_{i\sigma}(\tau')$$
$$+ S_{int}(i) \tag{A3}$$

constitutes the DMFT equations for the average local Green function $G_\sigma^{\mathrm{ave}}(\mathrm{i}\omega)$. For a single electron, equations (A2) and (A3) reduce, for the case without disorder, to the dynamical coherent-potential approximation (DCPA) equations (Sumi 1974) and, for the case without electron-phonon coupling, to the coherent-potential approximation (CPA) equations (Elliott *et al.* 1974).

For the pure Anderson model this is illustrated in figure A1. With increasing lattice coordination number K, we observe two effects. Firstly, the difference between the cavity and local Green functions indeed disappears, as can be seen from the vanishing of the bumps due to the van-Hove singularities; secondly, the LDOSs converge to the CPA density of states. Note also that Lifshitz tails, which are present within the statDMFT, also vanish, as expected, with increasing K.
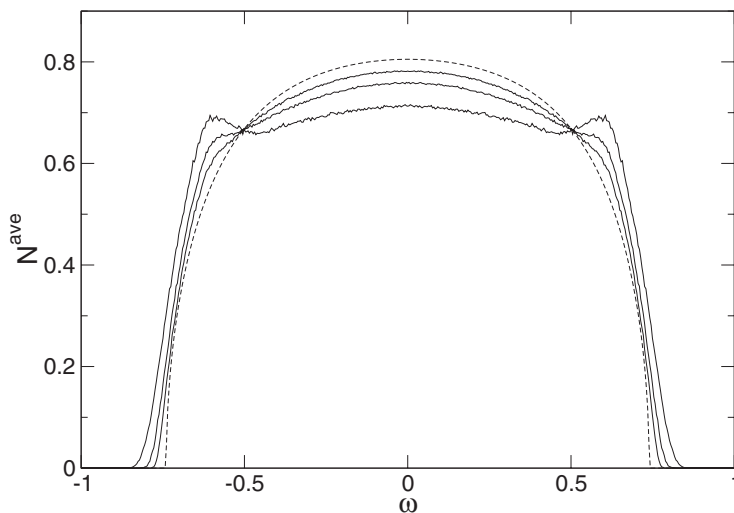
Figure A 1.   Average LDOS for the Bethe lattice with connectivity $K = 2, 4$ and 8 (—):
(- - -), the DMFT LDOS, that is the LDOS for $K \to \infty$.

REFERENCES

ABRAHAMS, E., ANDERSON, P. W., LICCIARDELLO, D. C., and RAMAKRISHNAN, T. V., 1979, *Phys. Rev. Lett.*, **42**, 673.

ABOU-CHACRA, R., ANDERSON, P. W., and THOULESS, D. J., 1973, *J. Phys.* C, **6**, 1734.

AGUIAR, M. C. O., MIRANDA, E., and DOBROSAVLJEVIĆ, V., 2003, *Phys. Rev.* B, **68**, 125104.

ALEXANDROV, A. S., KABANOV, V. V., and RAY, D. K., 1994, *Phys. Rev.* B, **49**, 9915.

ALEXANDROV, A. S., and KORNILOVITCH, P. E., 1999, *Phys. Rev. Lett.*, **82**, 807.

ALVERMANN, A., 2003, Diplom Thesis, Universität Bayreuth.

ANDERSON, P. W., 1958, *Phys. Rev.*, **109**, 1498; 1972, *Nature*, **235**, 163.

BAR-YAM, Y., EGAMI, T., MUSTRE-DE LEON, J., and BISHOP, A. R. (editors), 1992, *Lattice Effects in High-T_c Superconductors* (Singapore: World Scientific), pp. 377–422, and references therein.

BELITZ, D., and KIRKPATRICK, T. R., 1994, *Rev. mod. Phys.*, **66**, 261.

BONČA, J., TRUGMAN, S. A., and BATISTIĆ, I., 1999, *Phys. Rev.* B, **60**, 1633.

BREZINI, A., 1982, *J. Phys.* C, **15**, L211.

BREZINI, A., and OLIVIER, G., 1983, *Phil. Mag.* B, **47**, 461.

BREZINI, A., and ZERKI, N., 1992, *Phys. Stat. sol.* (b), **169**, 253.

BRONOLD, F. X., and FEHSKE, H., 2002, *Phys. Rev.* B, **66**, 073 102; 2003, *Acta Phys. Polonica*, **34**, 851.

BRONOLD, F. X., SAXENA, A., and BISHOP, A. R., 2001, *Phys. Rev.* B, **63**, 235 109.

CAPONE, M., STEPHAN, W., and GRILLI, M., 1997, *Phys. Rev.* B, **56**, 4484.

CASTELLANI, C., DI CASTRO, C., LEE, P. A., and MA, M., 1984, *Phys. Rev.* B, **30**, 527.

CHEONG, S.-W., HWANG, H. Y., CHEN, C. H., BATLOGG, B., RUPP, L. W., JR, and CARTER, S. A., 1994, *Phys. Rev.* B, **49**, 7088.

CIUCHI, S., DE PASQUALE, F., FRATINI, S., and FEINBERG, D., 1997, *Phys. Rev.* B, **56**, 4494.

COHEN, M. H., ECONOMOU, E. N., and SOUKOULIS, C. M., 1983, *Phys. Rev. Lett.*, **51**, 1202.

DERAEDT, H., and LAGENDIJK, A., 1983, *Phys. Rev.* B, **27**, 6097.

DOBROSAVLJEVIĆ, V., and KOTLIAR, G., 1997, *Phys. Rev. Lett.*, **78**, 3943; 1998, *Phil. Trans. R. Soc. Lond.* A, **356**, 1.

ECONOMOU, E. N., and COHEN, M. H., 1972, *Phys. Rev.* B, **5**, 2931.

ELLIOTT, R. J., KRUMHANSL, J. A., and LEATH, P. L., 1974, *Rev. mod. Phys.*, **46**, 465.

ELYUTIN, P. V., 1979, *Soviet Phys. Solid St.* **21**, 1590; 1981, *J. Phys.* C, **14**, 1435.

FEHSKE, H., LOOS, J., and WELLEIN, G., 1997a, *Z. Phys.* B, **104**, 619; 1997b, *Phys. Rev.* B, **56**, 4513; 2000, *Phys. Rev.* B, **61**, 8016.

FINKEL'STEIN, A. M., 1983, *Zh. eksp. teor. Fiz.*, **84**, 168 (Engl. transl., 1983, *Soviet Phys.* JETP, **57**, 97).

FIRSOV, Y. A., 1975, *Polarons* (Moscow: Nauka).

FLEISHMAN, L., and STEIN, D. L., 1979, *J. Phys.* C, **12**, 4817.

GEORGES, A., KOTLIAR, G., KRAUTH, W., and ROZENBERG, M. J., 1996, *Rev. mod. Phys.*, **68**, 13.

GIRVIN, S. M., and JONSON, M., 1980, *Phys. Rev.* B, **22**, 3583.

HEINRICHS, J., 1977, *Phys. Rev.* B, **16**, 4365.

HOLSTEIN, T., 1959, *Ann. Phys.* (*N.Y.*), **8**, 325–343.

JIN, S., TIEFEL, T. H., McCORMACK, M., FASTNACH, R. A., RAMESH, R., and CHEN, L. H., 1994, *Science*, **264**, 413.

KAMENEV, A., and ANDREEV, A., 1999, *Phys. Rev.* B, **60**, 2218.

KIRKPATRICK, T. R., and BELITZ, D., 1990, *J. Phys. condens. Mater*, **2**, 5259.

KOPIDAKIS, G., SOUKOULIS, C. M., and ECONOMOU, E. N., 1996, *Europhys. Lett.*, **33**, 459.

KRAMER, B., and MACKINNON, A., 1993, *Rep. Prog. Phys.*, **56**, 1469.

KUMAR, N., HEINRICHS, J., and KUMAR, A. A., 1975, *Solid St. Commun.*, **17**, 541.

LANDAU, L. D., 1933, *Z. Phys.*, **3**, 664.

LEE, P. A., and RAMAKRISHNAN, T. V., 1985, *Rev. mod. Phys.*, **57**, 287.

LOGAN, D. E., and WOLYNES, P. G., 1985, *Phys. Rev.* B, **31**, 2437; 1986, *J. chem. Phys.*, **85**, 937; 1987, *Phys. Rev.* B, **36**, 4135.

MAHAN, G., 1990, *Many-Particle Physics* (New York: Plenum).

MARSIGLIO, F., 1993, *Phys. Lett.* A, **180**, 280.

MILLER, J. D., and DERRIDA, B., 1993, *J. statist. Phys.*, **75**, 357.

MIRANDA, E., and DOBROSAVLJEVIĆ, V., 2001a, *Phys. Rev. Lett.*, **86**, 264; 2001b, *J. Magn. magn. Mater.*, **226–230**, 110.

MIRLIN, A., and FYODOROV, YAN, V., 1994, *J. Phys.*, *Paris*, I, **4**, 655.

MONTROLL, E. W., and SHLESINGER, M. F., 1983, *J. statist. Phys.*, **32**, 209.

MOTT, N. F., 1968a, *J. non-crystalline Solids*, **1**, 1; 1968b, *Phil. Mag.*, **22**, 7; 1976, *Commun. Phys.*, **1**, 203; 1981, *Phil. Mag.* B, **44**, 265.

MUELLER, H., and THOMAS, P., 1983, *Phys. Rev. Lett.*, **51**, 702.

OYANAGI, H., and BIANCONI, A. (editors), 2001, *Physics in Local Lattice Distortions: Fundamentals and Novel Concepts*, AIP Conference Proceeding, Vol. 554 (New York: American Institute of Physics).

PARRIS, P. E., KENKRE, V. M., and DUNLAP, D. H., 2001, *Phys. Rev. Lett.*, **87**, 126 601.

RANNINGER, J., and THIBBLIN, U., 1992, *Phys. Rev.* B, **45**, 7730.

RASHBA, E. I., 1982, *Excitons*, edited by E. I. Rashba and D. M. Sturge (Amsterdam: North-Holland), p. 542.

SALJE, E. K. H., ALEXANDROV, A. S., and LIANG, W. Y., 1995, *Polarons and Bipolarons in High-T_c Superconductors and Related Materials* (Cambridge: Cambridge University Press).

STEPHAN, W., 1996, *Phys. Rev.* B, **54**, 8981.

SUMI, H., 1974, *J. phys. Soc. Japan*, **36**, 770.

THOULESS, D. J., 1970, *J. Phys.* C, **3**, 1559; 1974, *Phys. Rep.*, **13**, 93.

TOKURA, Y., and TOMIOKA, Y., 1999, *J. Magn. magn. Mater.*, **200**, 1.

VOLLHARDT, D., and WÖLFLE, P., 1980, *Phys. Rev.* B, **22**, 4666; 1992, *Electronic Phase Transitions*, edited by W. Hanke and Yu. V. Kopaev (Amsterdam: North Holland) chap. 1, pp. 1–78.

VON OPPEN, F., WETTIG, T., and MÜLLER, J., 1996, *Phys. Rev. Lett.*, **76**, 491.

WEGNER, F. J., 1976, *Z. Phys.* B, **25**, 327.

WELLEIN, G., and FEHSKE, H., 1998, *Phys. Rev.* B, **58**, 6208.

WELLEIN, G., RÖDER, H., and FEHSKE, H., 1996, *Phys. Rev.* B, **52**, 9666.